catalysts

MDPI

Article

Solar-Assisted Hydroxyl Radical-Driven Photo-Fenton-like Catalytic Oxidation of Reactive Azo Dye Using an Iron-Based Metal–Organic Framework

M. M. Nour [1], Hossam A. Nabwey [1,*] and Maha A. Tony [2,3,*]

[1] College of Science and Humanities in Al-Kharj, Prince Sattam bin Abdulaziz University, Al-Kharj 11942, Saudi Arabia
[2] Advanced Materials/Solar Energy and Environmental Sustainability (AMSEES) Laboratory, Faculty of Engineering, Menoufia University, Shebin El-Kom 32511, Egypt
[3] Planning & Construction of Smart Cities Program, Faculty of Engineering, Menoufia National University, Menoufia 32651, Egypt
* Correspondence: eng_hossam21@yahoo.com (H.A.N.); dr.maha.tony@gmail.com (M.A.T.)

Abstract

The present study investigates the solar-assisted photo-Fenton-like degradation of a reactive azo dye (Red SPR) using an iron-based metal–organic framework, MIL-100(Fe), as a heterogeneous catalyst. The synthesized MIL-100(Fe) was successfully characterized by XRD, SEM, EDX, and FTIR analyses, confirming the formation of a crystalline, porous structure with well-dispersed Fe active sites. The catalytic performance was systematically evaluated under various operational parameters, including hydrogen peroxide dosage, catalyst loading, pH, circulation flow rate, initial dye concentration, and temperature. The results demonstrated that optimal degradation efficiency was achieved at pH 3.0, H_2O_2 concentration of 400 mg L^{-1}, and catalyst dosage of 40 mg L^{-1}, while a circulation flow rate of 400 mL min^{-1} ensured optimal hydrodynamic conditions. The system exhibited rapid degradation kinetics, achieving nearly complete dye removal within 60 min under solar irradiation. Kinetic analysis revealed that the degradation process follows pseudo-first-order behavior, with rate constants increasing from 0.1040 to 0.1589 min^{-1} as temperature increased from 25 to 55 °C. Thermodynamic analysis indicated that the process is endothermic ($\Delta H' = 8.72$ kJ mol^{-1}) and kinetically favorable with a low activation energy (Ea = 11.32 kJ mol^{-1}), while negative entropy values suggested the formation of an ordered transition state. Radical scavenger experiments confirmed that hydroxyl radicals (•OH) are the dominant reactive species, with secondary contributions from superoxide radicals ($O_2•^-$). The enhanced performance is attributed to the synergistic effect of solar irradiation and Fe^{3+}/Fe^{2+} redox cycling within the MIL-100(Fe) framework. Hence, the study demonstrates that MIL-100(Fe) is a highly efficient and sustainable catalyst for solar-driven wastewater treatment applications.

Keywords: MIL-100(Fe); reactive oxygen species; azo dye; heterogeneous catalysis; oxidation; solar-assisted photo-Fenton

Check for updates

Academic Editors: Yunfeng Ma, Peng Lu and Xiaole Weng

Received: 20 April 2026
Revised: 15 May 2026
Accepted: 19 May 2026
Published: 26 May 2026

Copyright: © 2026 by the authors. Licensee MDPI, Basel, Switzerland. This article is an open access article distributed under the terms and conditions of the Creative Commons Attribution (CC BY) license.

1. Introduction

The increasing discharge of synthetic dyes from textile and related industries poses a serious environmental challenge due to their toxicity, persistence, and resistance to conventional treatment methods [1,2]. Among these pollutants, reactive azo dyes are

particularly problematic because of their complex aromatic structures and the presence of azo (–N=N–) bonds, which impart high chemical stability and low biodegradability [3–5]. In addition, many reactive dyes exhibit high water solubility due to the presence of sulfonate groups, facilitating their rapid dispersion in aquatic systems and making their removal more challenging [6,7]. The accumulation of such dyes in water bodies not only reduces light penetration but also leads to the formation of toxic and potentially carcinogenic by-products [3,8–11].

Conventional wastewater treatment methods, including coagulation–flocculation, adsorption, membrane filtration, and biological processes, have been widely applied for dye removal. Coagulation–flocculation is effective for removing suspended dye particles [2,6]; however, it often generates large volumes of secondary sludge that require further treatment and disposal [12–14]. Adsorption techniques, particularly those employing activated carbon, offer high removal efficiency but are limited by high operational costs and challenges associated with adsorbent regeneration [5,15]. Membrane-based technologies provide excellent separation performance, yet they suffer from membrane fouling, high energy consumption, and significant maintenance requirements [16,17]. Biological treatments, although environmentally friendly and cost-effective, are generally inefficient for degrading reactive azo dyes due to their complex molecular structures and resistance to microbial degradation [9,18–22]. Consequently, these conventional approaches often result in incomplete dye removal or merely transfer pollutants from one phase to another rather than achieving complete mineralization, highlighting the need for more advanced and sustainable treatment technologies [23].

Advanced oxidation processes (AOPs) have emerged as promising alternatives for the degradation of refractory organic contaminants. Among these, the Fenton and photo-Fenton processes have attracted considerable attention due to their ability to generate highly reactive hydroxyl radicals (•OH), which can non-selectively oxidize a wide range of organic pollutants into harmless end products such as CO_2 and H_2O [24–26]. Nevertheless, conventional homogeneous Fenton systems suffer from several limitations, including a narrow operational pH range, the formation of iron sludge, and difficulties in catalyst recovery, which hinder their large-scale application [27,28].

To address these challenges, heterogeneous Fenton-like systems based on solid catalysts have been extensively explored. In this regard, iron-based metal–organic frameworks (MOFs) have emerged as highly promising materials owing to their high surface area, tunable porosity, and well-dispersed active metal sites [6,29–31]. Among them, MIL-100(Fe), constructed from Fe^{3+} clusters and benzene-1,3,5-tricarboxylate (BTC) linkers, has demonstrated excellent catalytic activity in oxidation reactions. Its mesoporous structure enhances mass transfer, while the accessible iron centers facilitate the efficient activation of hydrogen peroxide for the generation of reactive oxygen species [32–36]. Furthermore, the incorporation of light irradiation in photo-Fenton-like processes, particularly under solar illumination [37], significantly enhances catalytic performance by accelerating the Fe^{3+}/Fe^{2+} redox cycle and promoting additional radical generation [38–41]. This solar-driven approach offers a sustainable and energy-efficient pathway for wastewater treatment by utilizing abundant renewable energy while improving degradation kinetics and mineralization efficiency [8,42–47].

The novelty of the present study lies in the development of a solar-assisted heterogeneous photo-Fenton system based on MIL-100(Fe) for the efficient degradation of the reactive azo dye Red SPR under natural solar irradiation. The synergistic interaction between solar irradiation and the Fe^{3+}/Fe^{2+} redox cycle within the MIL-100(Fe) framework significantly enhances reactive oxygen species generation and improves dye degradation efficiency. In contrast to conventional homogeneous Fenton systems, the developed pro-

cess minimizes iron sludge formation while facilitating catalyst recovery and improving process sustainability. Moreover, the mesoporous structure and accessible Fe active sites of MIL-100(Fe) promote efficient H_2O_2 activation and pollutant oxidation. Furthermore, this study provides mechanistic insight into the solar photo-Fenton degradation process through radical scavenger tests, iron leaching analysis, and kinetic and thermodynamic investigations. In addition, the integration of MIL-100(Fe) with a recirculating parabolic trough solar reactor demonstrates the potential of this system for efficient reactive azo dye degradation under natural solar irradiation.

2. Results and Discussion

2.1. XRD Characterization

The crystalline structure of the synthesized material was examined by X-ray diffraction (XRD), and the resulting pattern is presented in Figure 1. The diffractogram exhibits a series of well-defined reflections, confirming the formation of a crystalline and structurally ordered framework. The XRD pattern displays the characteristic diffraction peaks of MIL-100(Fe), particularly in the low-angle region, which is typical for metal–organic frameworks with large unit cells and highly porous architectures. The prominent reflections observed at 2θ about 9.5°, 11.3°, 17.5°, and 19.8° can be indexed to the (220), (311), (400), and (331) crystallographic planes, respectively. Among these, the intense peak at 11.3° corresponding to the (311) plane is considered the diagnostic reflection of MIL-100(Fe), confirming the successful formation of the cubic framework. These major diffraction peaks are consistent with the crystallographic data reported for MIL-100(Fe) (CCDC No. 640536) [39–41].

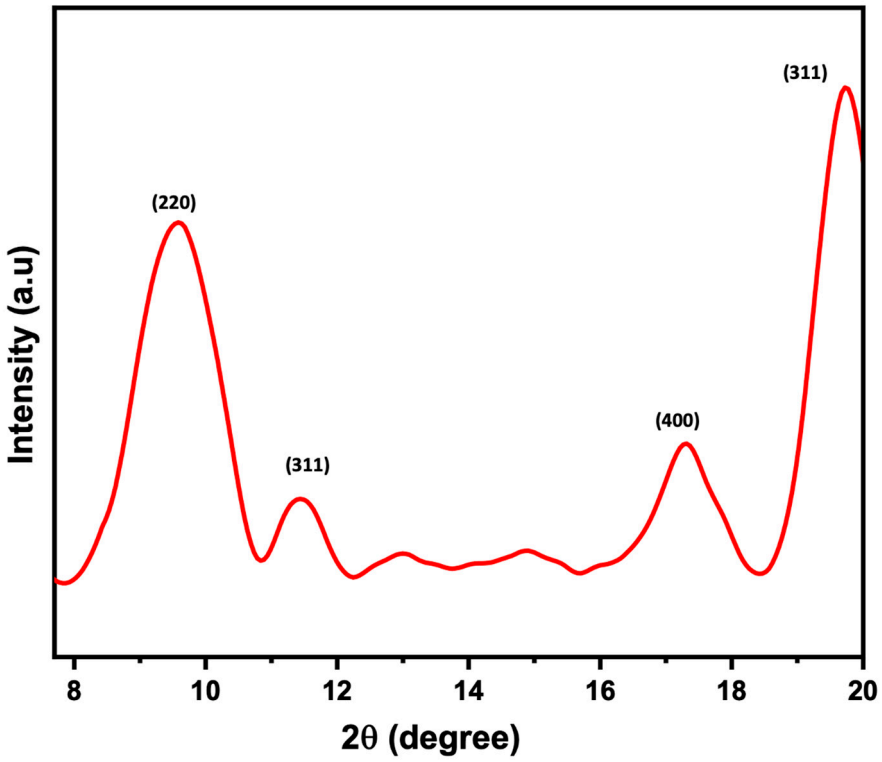


Figure 1. X-ray diffraction pattern of the synthesized MIL-100(Fe).

Additional weaker reflections observed at higher diffraction angles further support the preservation of the ordered framework structure. The overall peak positions and distribution are in good agreement with previously reported XRD patterns of MIL-100(Fe), which consists of trinuclear Fe_3O clusters interconnected by 1,3,5-benzenetricarboxylate (BTC) linkers, forming a three-dimensional mesoporous network. Thus, no characteristic

diffraction peaks corresponding to crystalline iron oxide phases (such as hematite or magnetite) are detected, indicating that iron species are well incorporated within the MOF framework rather than existing as separate phases. The slight broadening of some peaks suggests relatively small crystallite size and partial structural disorder, which is commonly observed in MIL-type materials synthesized under controlled conditions.

2.2. SEM Morphology Description of MIL-100(Fe)

Figure 2a illustrates the surface morphology of the synthesized MIL-100(Fe) at low magnification, revealing the formation of irregularly shaped aggregates composed of densely packed particles. The material exhibits a characteristic hierarchical structure, where primary nanoparticles are assembled into larger secondary clusters. Although well-defined polyhedral crystals typically reported for ideal MIL-100(Fe) are not distinctly observed, the presence of aggregated domains suggests partial crystallization accompanied by structural disorder, which is commonly influenced by synthesis conditions such as pH, temperature, and precursor concentration. The overall morphology indicates a loosely compacted framework with interparticle voids that can facilitate diffusion processes.

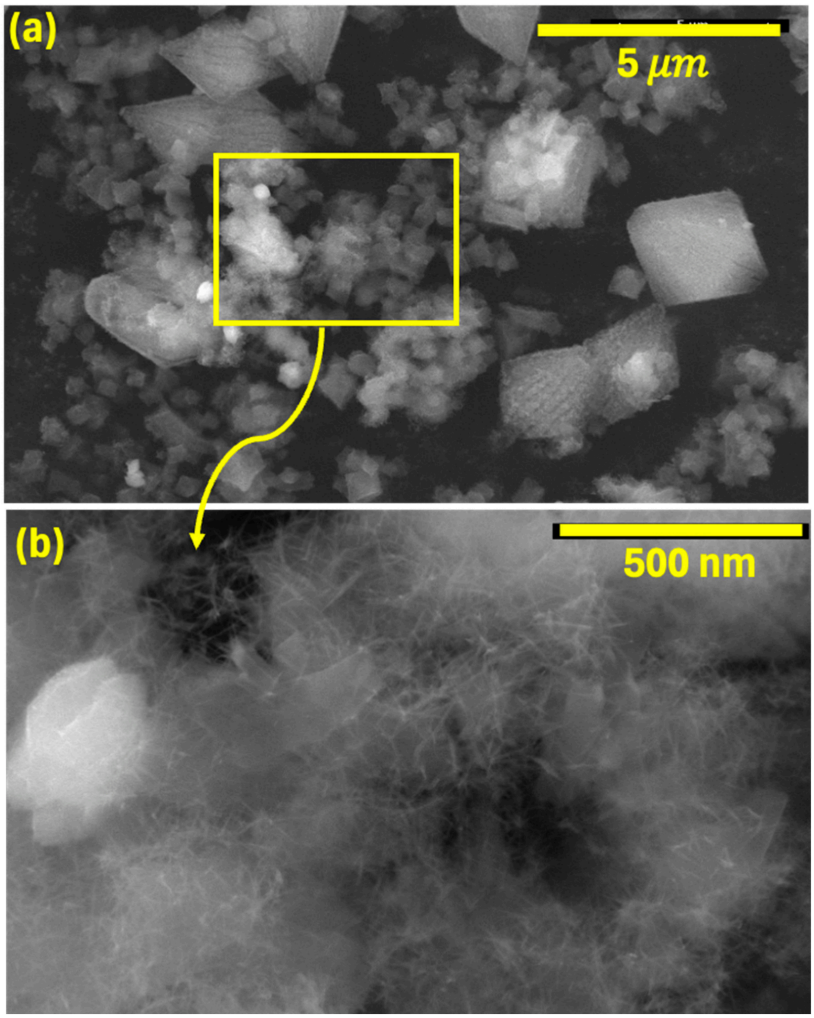


Figure 2. SEM Characterization of MIL-100(Fe) morphology at (**a**) low and (**b**) high magnification.

Figure 2b, recorded at higher magnification (scale bar: 500 nm), provides a closer view of the surface architecture, highlighting a rough and highly porous texture. The micrograph reveals an interconnected network of nanosized particles forming a sponge-like structure with abundant mesoporous and macroporous features. These pores likely originate from

the intrinsic porous cages of MIL-100(Fe) combined with intercrystalline voids created during particle aggregation. The surface appears uneven with noticeable cavities and channels, which are essential for enhancing reactant accessibility and promoting mass transfer during catalytic reactions.

Additionally, contrast variations within the image, particularly the brighter regions, may be attributed to localized densification or Fe-rich clusters within the framework. The absence of smooth crystal facets further suggests that the material possesses a semi-crystalline nature with a high density of structural defects, which can act as active sites in Fenton-like catalytic processes. Hence, the SEM observations confirm that MIL-100(Fe) exhibits a hierarchically porous and aggregated nanostructure with significant surface roughness and interconnected pore channels. This morphology is highly advantageous for heterogeneous photo-Fenton applications, as it enhances the dispersion of active Fe sites, facilitates efficient interaction with H_2O_2, and improves the generation and diffusion of reactive oxygen species.

2.3. EDX and Elemental Mapping Analysis

The elemental composition and spatial distribution of the synthesized MIL-100(Fe) were investigated using energy-dispersive X-ray spectroscopy (EDX) coupled with SEM elemental mapping, as illustrated in Figure 3a–f. The complete EDX spectrum shown in Figure 3a exhibited the characteristic signals corresponding to Fe, O, and C, confirming the successful formation of the Fe-based metal–organic framework. The strong Fe peaks observed at approximately 7.06 keV and 7.84 keV are attributed to Fe Kα and Fe Kβ emissions, respectively, indicating the successful incorporation of iron species within the framework structure. In addition, the peaks corresponding to C and O are associated with the aromatic carbon backbone and oxygen-containing carboxylate groups of the trimesic acid (BTC) organic linker.

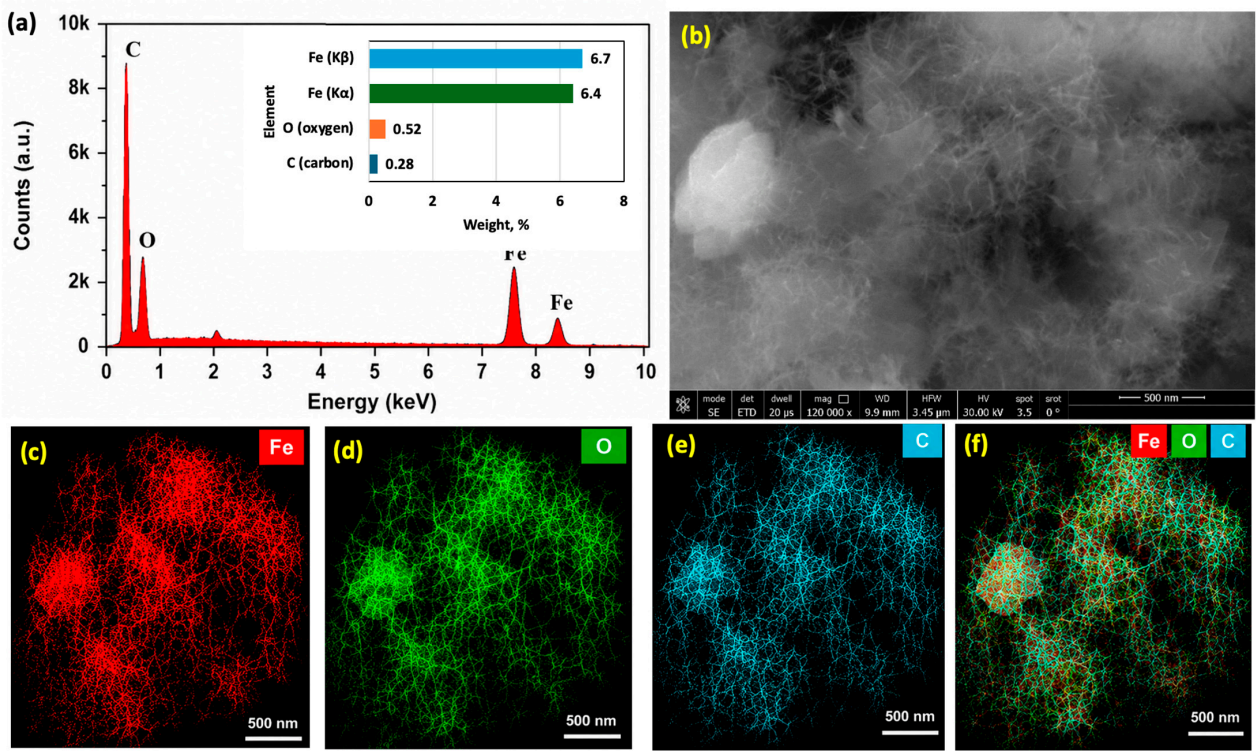


Figure 3. SEM–EDX characterization of MIL-100(Fe): (**a**) complete EDX spectrum with elemental composition inset showing the characteristic peaks of Fe, O, and C, (**b**) SEM micrograph, (**c**) Fe elemental map, (**d**) O elemental map, (**e**) C elemental map, and (**f**) overlay elemental distribution map.

The SEM image presented in Figure 3b reveals the agglomerated fibrous-like morphology of the synthesized MIL-100(Fe). Furthermore, the elemental mapping images shown in Figure 3c–e demonstrate the homogeneous spatial distribution of Fe, O, and C throughout the material surface without noticeable elemental segregation or localized agglomeration. The overlay image in Figure 3f further confirms the uniform dispersion of the constituent elements across the framework structure. Moreover, no additional elemental signals corresponding to foreign impurities or residual precursor species were detected, indicating the high purity of the synthesized MIL-100(Fe). These results provide strong evidence for the successful synthesis and compositional homogeneity of the prepared MOF catalyst.

2.4. FTIR Analysis

The FTIR spectrum of the synthesized MIL-100(Fe) provides strong evidence for the successful formation of the Fe-based metal–organic framework through coordination between Fe^{3+} ions and the trimesate ligand, as presented in Figure 4. A broad absorption band centered at approximately 3400 cm^{-1} is attributed to the O–H stretching vibration of physically adsorbed and coordinated water molecules confined within the porous framework structure.

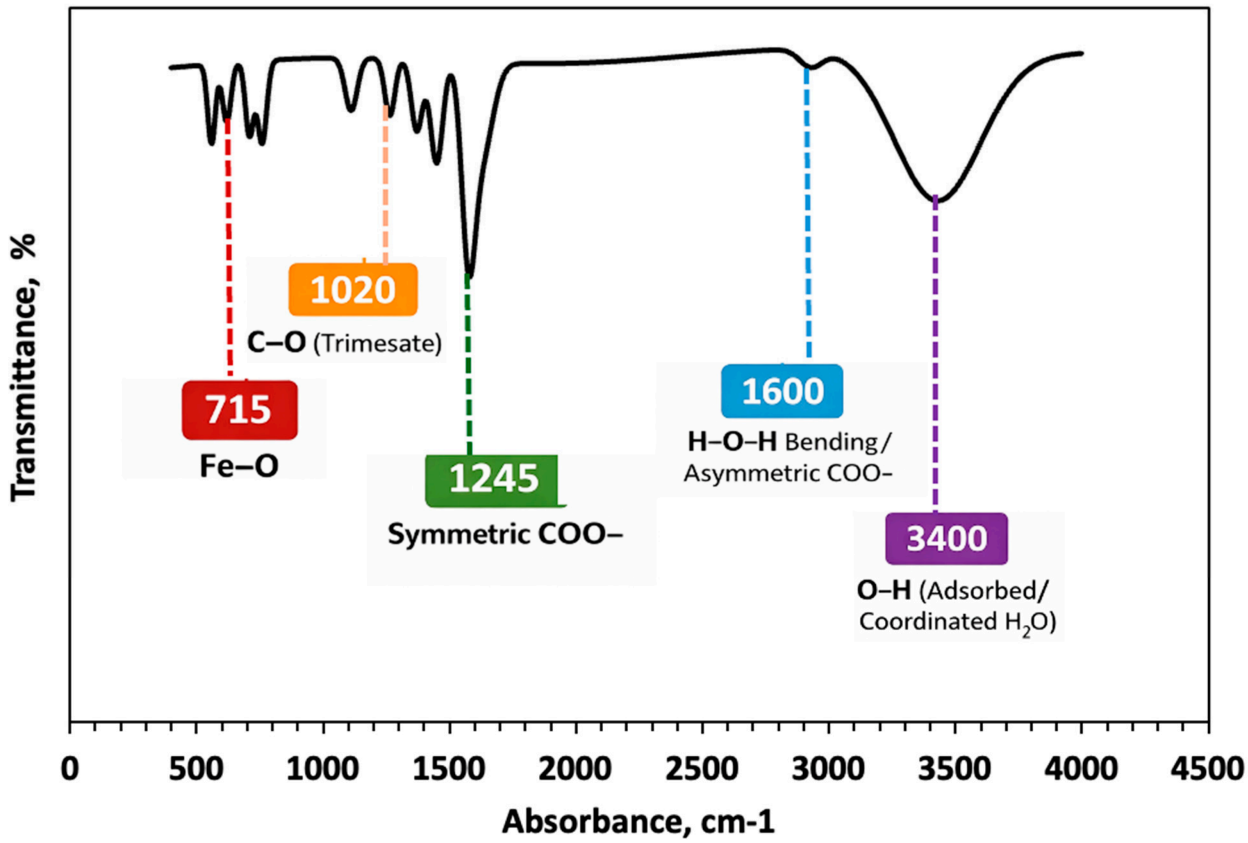


Figure 4. FTIR spectrum of the synthesized MIL-100(Fe) showing characteristic vibrations of the organic linker and Fe–O coordination bonds.

The absorption band observed near 1600 cm^{-1} corresponds primarily to the H–O–H bending vibration of adsorbed/coordinated water molecules and partially overlaps with the asymmetric stretching vibration of coordinated carboxylate groups (COO^{-}). This overlap indicates the interaction between the trimesate ligand and Fe centers within the framework structure. To further clarify the carboxylate coordination behavior, the symmetric stretching vibration of COO^{-} groups is separately identified by the bands appearing within the 1450–1380 cm^{-1} region. The separation between the asymmetric and symmetric

COO^- stretching vibrations confirms the formation of coordination bonds between the carboxylate groups of trimesic acid and Fe^{3+} ions, demonstrating successful MOF framework construction.

Moreover, the peaks observed between 1100 and 1250 cm^{-1} are assigned to the C–O stretching vibrations of the trimesate organic linker, indicating preservation of the ligand structure after coordination. In the low-wavenumber region (700–500 cm^{-1}), distinct absorption bands corresponding to Fe–O stretching vibrations are detected, providing additional evidence for the formation of Fe–O clusters characteristic of MIL-100(Fe). Overall, the FTIR results confirm the successful synthesis of a well-coordinated Fe-based MOF structure possessing coordinated metal centers and preserved organic functionality.

2.5. BET Surface Area and Porosity Analysis

The textural properties of the synthesized MIL-100(Fe) were investigated using BET surface area analysis. The obtained results revealed a specific surface area of 736 $m^2\ g^{-1}$ and a pore volume of 0.28 $cm^3\ g^{-1}$, confirming the porous nature of the synthesized MIL-100(Fe) framework. The relatively high surface area and porous structure are beneficial for heterogeneous photo-Fenton applications, as they provide abundant accessible active sites and facilitate the diffusion of dye molecules and reactive oxygen species within the MOF structure. These porous characteristics contribute significantly to the enhanced catalytic performance observed during the solar-assisted degradation of Red SPR dye.

2.6. Catalytic Degradation of Dye Wastewater

2.6.1. Comparison of Degradation Performance with and Without MIL-100(Fe)

To assess the catalytic contribution of MIL-100(Fe), a comparative study was conducted to evaluate the degradation performance of the solar photo-Fenton system in the absence and presence of the MOF catalyst, as illustrated in Figure 5. This Figure clearly demonstrates the significant enhancement in Red SPR dye degradation upon incorporation of MIL-100(Fe) into the solar photo-Fenton system. In the absence of the catalyst, the degradation process proceeds at a considerably slower rate, achieving limited removal efficiency due to the relatively low generation of reactive oxygen species (ROS) under homogeneous conditions. In contrast, the presence of MIL-100(Fe) markedly accelerates the degradation kinetics, resulting in substantially higher removal efficiency within the same reaction time. Such enhanced performance can be attributed to the unique structural and catalytic properties of MIL-100(Fe). The MOF provides a high surface area and abundant accessible Fe active sites, which facilitate the efficient decomposition of hydrogen peroxide (H_2O_2) into highly reactive hydroxyl radicals (•OH). Moreover, the heterogeneous Fe^{3+}/Fe^{2+} redox cycling within the MIL-100(Fe) framework is further promoted under solar irradiation, leading to continuous ROS generation and improved catalytic turnover.

In addition, MIL-100(Fe) enhances the adsorption of dye molecules onto its porous structure, increasing the local concentration of pollutants near the active sites and promoting effective oxidation. The synergistic interaction between adsorption and catalytic oxidation contributes to the superior degradation efficiency observed in the MOF-assisted system.

Conversely, in the absence of MIL-100(Fe), the process relies primarily on homogeneous Fenton reactions, which are limited by slower Fe redox cycling and lower radical production efficiency. This results in reduced degradation rates and incomplete pollutant removal. Therefore, the results confirm that MIL-100(Fe) plays a crucial role in enhancing the efficiency of the solar photo-Fenton process, enabling faster degradation kinetics and higher removal efficiency compared to systems without the catalyst [45,46]. These findings are consistent with recent studies [43,44] on Fe-based MOFs, where MIL-100(Fe) and similar

materials have demonstrated significantly improved photo-Fenton activity compared to conventional systems. Previous reports indicate that MOF-based catalysts enhance ROS generation, improve light utilization, and reduce iron leaching, thereby outperforming traditional homogeneous Fenton processes in dye degradation applications.

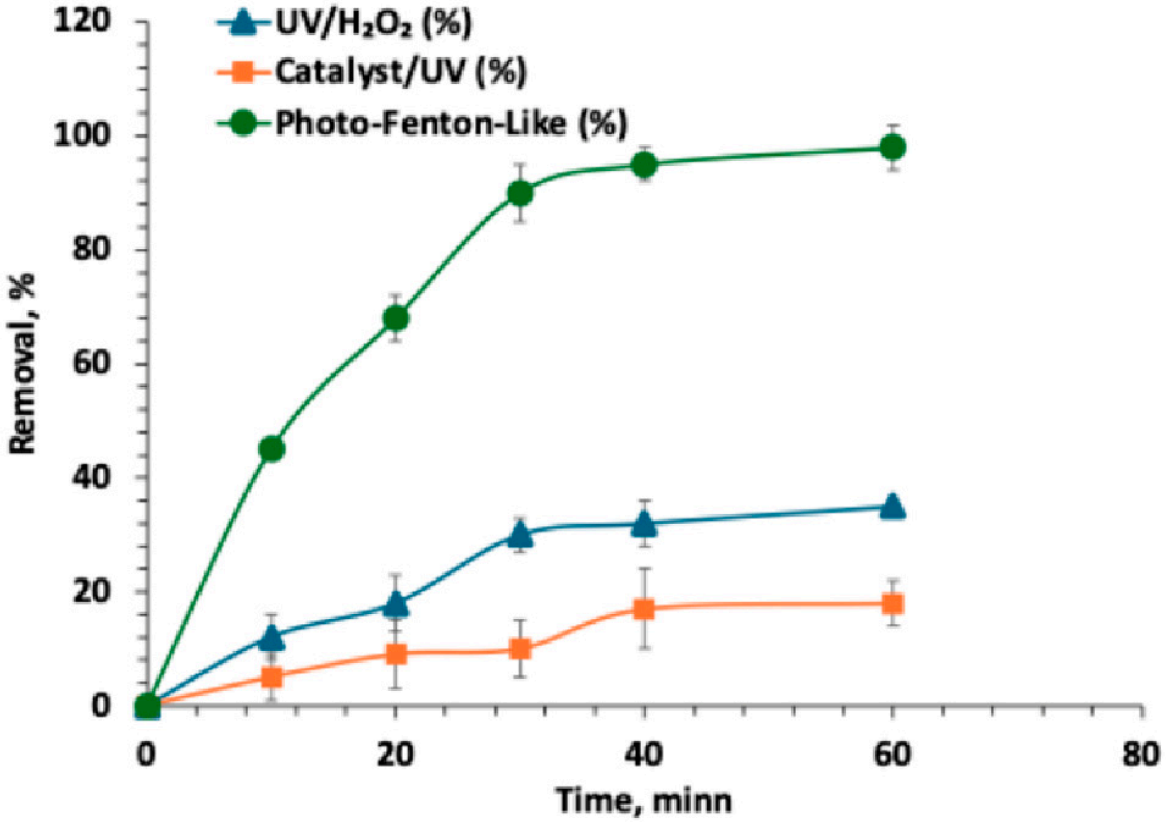


Figure 5. Comparative evaluation of Red SPR dye degradation in the absence and presence of MIL-100(Fe) under solar photo-Fenton conditions (pH 3.0, H_2O_2 = 400 mg L^{-1}, Fe = 40 mg L^{-1}).

2.6.2. Effect of Hydrogen Peroxide Dose

Figure 6 illustrates the influence of H_2O_2 concentration (200, 400, and 600 mg L^{-1}) on the degradation performance of the MIL-100(Fe)-based solar photo-Fenton system. The results clearly demonstrate that increasing the H_2O_2 dose enhances the degradation efficiency up to an optimum level, beyond which no significant improvement is observed. At 200 mg L^{-1}, the degradation rate was relatively moderate, achieving approximately 75% removal at 20 min and ~95% after 60 min. Increasing the H_2O_2 concentration to 400 mg L^{-1} significantly improved the degradation efficiency, reaching ~85% at 20 min and nearly complete removal (~99%) after 60 min, indicating enhanced generation of hydroxyl radicals (•OH). However, a further increase to 600 mg L^{-1} resulted in only a slight improvement in the early stage (78% at 20 min) and ultimately achieved ~96–97% removal at 60 min, showing no substantial benefit compared to 400 mg L^{-1}. The observed enhancement at moderate H_2O_2 dosage (400 mg L^{-1}) is attributed to the increased production of •OH radicals through the Fenton and photo-Fenton reactions, thereby accelerating dye oxidation. However, at excessive H_2O_2 concentrations (600 mg L^{-1}), the degradation efficiency does not improve proportionally due to the self-scavenging effect of H_2O_2, where excess peroxide reacts with •OH radicals to produce weaker oxidizing species such as HO_2• (Equation (3)), reducing the effective radical concentration available for dye degradation [27,48].

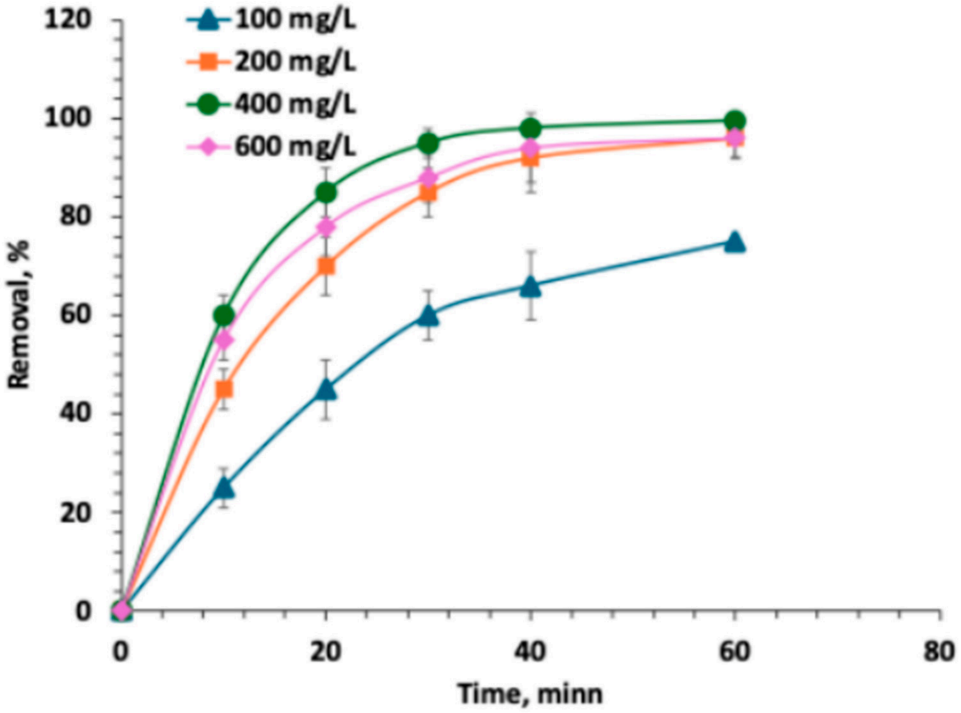


Figure 6. Effect of hydrogen peroxide concentration (200–600 mg L^{-1}) on the solar photo-Fenton degradation of Red SPR dye using MIL-100(Fe) under fixed operating conditions (pH 3.0, Fe = 40 mg L^{-1}).

Additionally, excess H_2O_2 may compete with dye molecules for active sites on the MIL-100(Fe) surface and contribute to non-productive decomposition pathways, further limiting system efficiency. This explains why the performance at 600 mg L^{-1} does not surpass that at 400 mg L^{-1} despite the higher oxidant dosage. Importantly, while 400 mg L^{-1} yields the maximum catalytic performance, increasing the H_2O_2 concentration to 600 mg L^{-1} provides no substantial enhancement due to radical scavenging by excess peroxide. Consequently, 400 mg L^{-1} is considered the optimal dosage from both kinetic and techno-economic perspectives. Such investigation is consistent with and in accordance with previous studies [28,49] on Fenton and MOF-based photo-Fenton systems, where an optimum H_2O_2 concentration is commonly observed. Excess oxidant has been reported to reduce degradation efficiency due to radical scavenging and recombination effects, while insufficient H_2O_2 limits ROS generation.

2.6.3. Effect of MOF Dose

To evaluate the influence of catalyst loading on the degradation performance, the effect of MIL-100(Fe) dosage on the solar photo-Fenton oxidation of Red SPR dye was investigated, as shown in Figure 7. Figure 7 illustrates the effect of MIL-100(Fe) dosage in the range of 20–80 mg L^{-1} on the degradation efficiency of Red SPR dye. The results clearly indicate that increasing the MOF dose significantly enhances the degradation rate up to an optimum level, beyond which only marginal improvement is observed. At the lowest catalyst loading (20 mg L^{-1}), the degradation process was relatively slow, achieving only ~50% removal within 20 min and ~85% after 60 min. Upon increasing the dose to 40 mg L^{-1}, the degradation efficiency improved markedly, reaching ~75% at 20 min and ~96% at 60 min. A further increase to 60 mg L^{-1} resulted in the highest performance, with ~85% removal achieved within 20 min and nearly complete degradation (~99%) after 60 min. However, increasing the catalyst dose to 80 mg L^{-1} did not significantly enhance the removal efficiency, with ~93–94% removal at 60 min, indicating a plateau behavior.

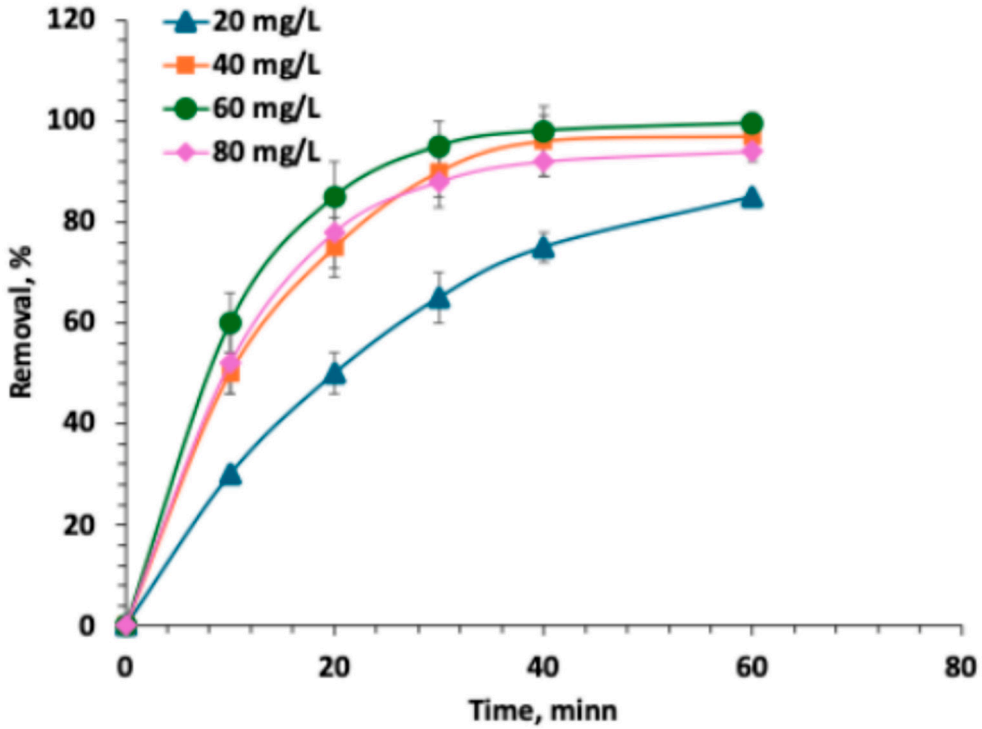


Figure 7. Effect of MIL-100(Fe) dosage (20–80 mg L^{-1}) on the solar photo-Fenton degradation of Red SPR dye under fixed operating conditions (pH 3.0, H_2O_2 = 400 mg L^{-1}).

The enhancement in degradation efficiency at higher MOF dosages can be attributed to the increased availability of active Fe sites within the MIL-100(Fe) framework, which promotes the decomposition of H_2O_2 into highly reactive hydroxyl radicals (•OH). This leads to a higher rate of ROS generation and improved catalytic activity. Additionally, higher catalyst loading increases the surface area and adsorption capacity for dye molecules, facilitating better interaction between pollutants and active sites. However, the slight decline or plateau observed at excessive catalyst loading (80 mg L^{-1}) can be explained by several factors. First, increased turbidity of the suspension at higher catalyst concentrations may hinder light penetration, reducing the effective photoactivation of the catalyst. Second, excess iron species may act as radical scavengers, leading to non-productive consumption of hydroxyl radicals. Third, particle agglomeration at higher dosages may reduce the effective surface area and limit active site accessibility. Notably, although 60 mg L^{-1} yields the maximum catalytic performance, the limited gain over 40 mg L^{-1} does not justify the increased catalyst usage, making 40 mg L^{-1} the preferred dosage from a techno-economic standpoint. These observations are consistent with previous studies [29,48] on MIL-100(Fe)-based photo-Fenton systems. For example, hybrid MIL-100(Fe) catalysts have shown enhanced degradation efficiency with increasing catalyst dosage up to an optimum level, beyond which no significant improvement is observed due to light scattering and radical recombination effects. Similarly, other Fe-based MOF systems have demonstrated that an optimal catalyst loading is essential to balance ROS generation and light utilization efficiency, with excessive dosages leading to diminished performance.

2.6.4. Effect of Operating pH

Figure 8 demonstrates the significant influence of solution pH on the degradation efficiency of Red SPR dye using the MIL-100(Fe)-based solar photo-Fenton system. The results reveal that the degradation process is highly pH-dependent, with maximum efficiency achieved under acidic conditions, particularly at pH 3.0. This can be explained by the fact that at pH 3, the system exhibited the highest degradation rate and removal efficiency,

indicating optimal conditions for hydroxyl radical (•OH) generation. This behavior is attributed to the enhanced redox cycling between Fe^{2+} and Fe^{3+} within the MIL-100(Fe) framework, which promotes efficient decomposition of H_2O_2 into reactive oxygen species (ROS). Under these conditions, iron remains in a soluble and catalytically active form, facilitating continuous radical production and rapid oxidation of dye molecules [48]. However, at higher pH values (neutral and alkaline conditions), a significant decline in degradation efficiency is typically observed. This reduction can be attributed to several factors, including the precipitation of iron species as ferric hydroxides ($Fe(OH)_3$), which reduces the availability of active Fe sites. Additionally, the decomposition of H_2O_2 into non-reactive species, including O_2 and H_2O, is favored at higher pH, leading to lower •OH generation efficiency. Furthermore, hydroxyl radicals may undergo recombination or scavenging reactions under alkaline conditions, reducing their availability for pollutant degradation.

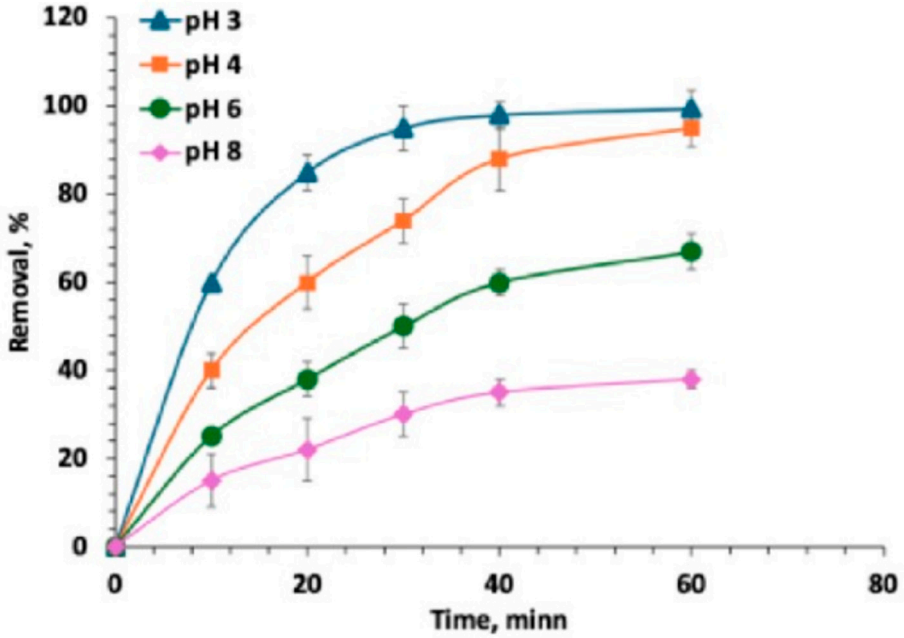


Figure 8. Effect of initial solution pH on the solar photo-Fenton degradation of Red SPR dye using MIL-100(Fe) under fixed operating conditions (H_2O_2 = 400 mg L^{-1}, MOF = 40 mg L^{-1}).

In contrast, at very low pH values (pH < 3), the degradation efficiency may also decrease slightly due to the stabilization of H_2O_2 as oxonium ions ($H_3O_2^+$), which reduces its reactivity with Fe^{2+}. Therefore, pH 3 represents an optimal balance between catalyst activity, oxidant efficiency, and radical generation. These findings are consistent with numerous studies [5,26,28,44] on Fenton and photo-Fenton systems, where pH 2.5–3.5 is widely reported as the optimal range for maximum degradation efficiency. Similar trends have been observed in Fe-based MOF systems, including MIL-100(Fe), where acidic conditions enhance catalytic performance while maintaining structural stability.

2.6.5. Effect of Circulation Flow Rate

To evaluate the influence of hydrodynamic conditions on reactor performance, the effect of circulation flow rate on the solar photo-Fenton degradation of Red SPR dye was investigated, as shown in Figure 9. Figure 9 demonstrates a pronounced influence of circulation flow rate on the degradation efficiency of Red SPR dye. Increasing the flow rate from 200 to 400 mL min^{-1} significantly enhances the degradation performance. At 200 mL min^{-1}, the system shows comparatively slower kinetics, with moderate removal efficiency over time. Upon increasing the flow rate to 300 mL min^{-1}, the degradation improves

noticeably, indicating enhanced mass transfer and better distribution of reactants within the reactor. The highest degradation efficiency is achieved at 400 mL min^{-1}, where the system reaches nearly complete removal (about 99%) within 60 min. This improvement can be attributed to optimized hydrodynamic conditions, which promote uniform dispersion of MIL-100(Fe) particles, efficient mixing of H_2O_2 and dye molecules, and enhanced exposure of the reaction medium to solar irradiation. As a result, the generation and utilization of reactive oxygen species (ROS), particularly hydroxyl radicals (•OH), are maximized.

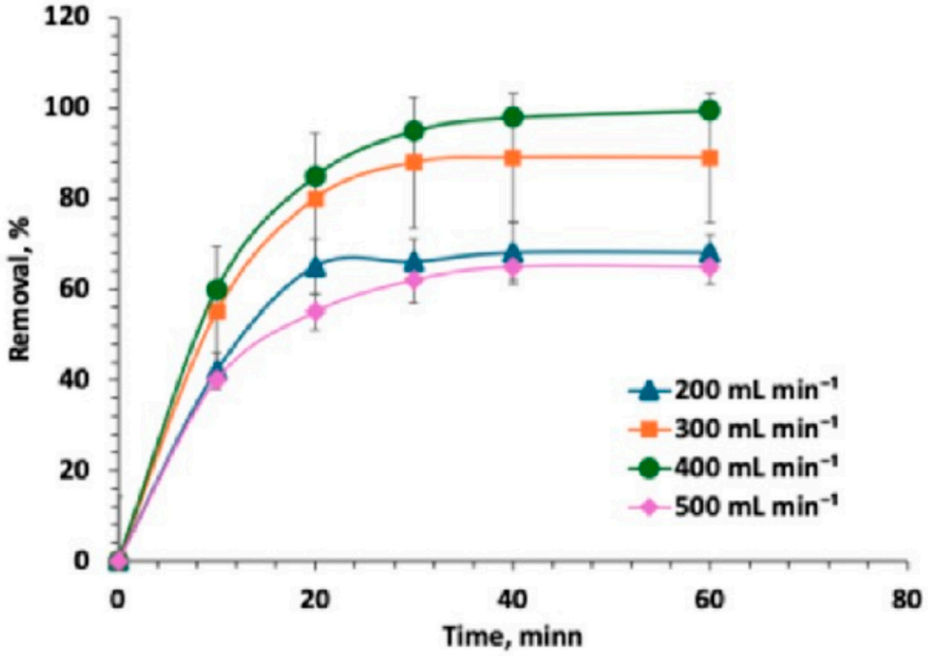


Figure 9. The impact of circulation flow rate on the degradation efficiency of Red SPR dye in the MIL-100(Fe)-based solar photo-Fenton system (H_2O_2 = 400 mg L^{-1}, MOF = 40 mg L^{-1}, pH 3.0, Dye 20 mg/L).

However, a further increase in flow rate to 500 mL min^{-1} leads to a slight decline in degradation efficiency. Although higher flow rates improve turbulence and mixing, they simultaneously reduce the residence time of the reaction mixture within the illuminated zone of the reactor. This limits the effective interaction time between ROS and dye molecules, resulting in reduced overall degradation efficiency [5]. Additionally, excessive flow may lead to inefficient photon utilization due to rapid fluid movement [16]. Thus, it is essential to mention that while increasing the circulation flow rate enhances mixing and photon utilization, excessive flow reduces effective irradiation time, confirming that 400 mL min^{-1} is the optimal and operationally efficient flow rate for achieving maximum degradation efficiency in this system. These findings confirm the existence of an optimal flow rate, where a balance is achieved between mass transfer enhancement and sufficient irradiation time. Similar trends have been reported in solar photoreactor systems, where moderate flow rates maximize degradation efficiency, while excessively high flow rates reduce performance due to shortened residence time and incomplete radical utilization.

2.6.6. Effect of Initial Dye Loading

To investigate the influence of pollutant loading on the degradation efficiency, the effect of the initial concentration of Red SPR dye was evaluated in the range of 20–50 mg L^{-1}, as presented in Figure 10. The Figure illustrates that increasing the initial dye concentration from 20 to 50 mg L^{-1} results in a systematic decrease in degradation efficiency over the reaction time. At an initial concentration of 20 mg L^{-1}, the system achieved rapid degrada-

tion, reaching approximately 68% removal within 20 min and up to 97% after 60 min. In contrast, at 30 mg L^{-1}, the removal efficiency slightly decreased to 60% at 20 min and 93% after 60 min. A more pronounced decline was observed at higher concentrations, where 40 mg L^{-1} exhibited 50% removal at 20 min and 88% at 60 min, while the highest tested concentration (50 mg L^{-1}) showed only 40% removal at 20 min and reached 78% after 60 min. This trend clearly demonstrates that lower initial dye concentrations favor faster degradation kinetics and higher overall removal efficiency. The observed behavior can be primarily attributed to the light attenuation (shadowing) effect, where increasing dye concentration intensifies solution color, thereby limiting solar radiation penetration and reducing the activation of the MIL-100(Fe) catalyst. Consequently, the photoreduction of Fe^{3+} to Fe^{2+} and the generation of hydroxyl radicals (•OH) are suppressed.

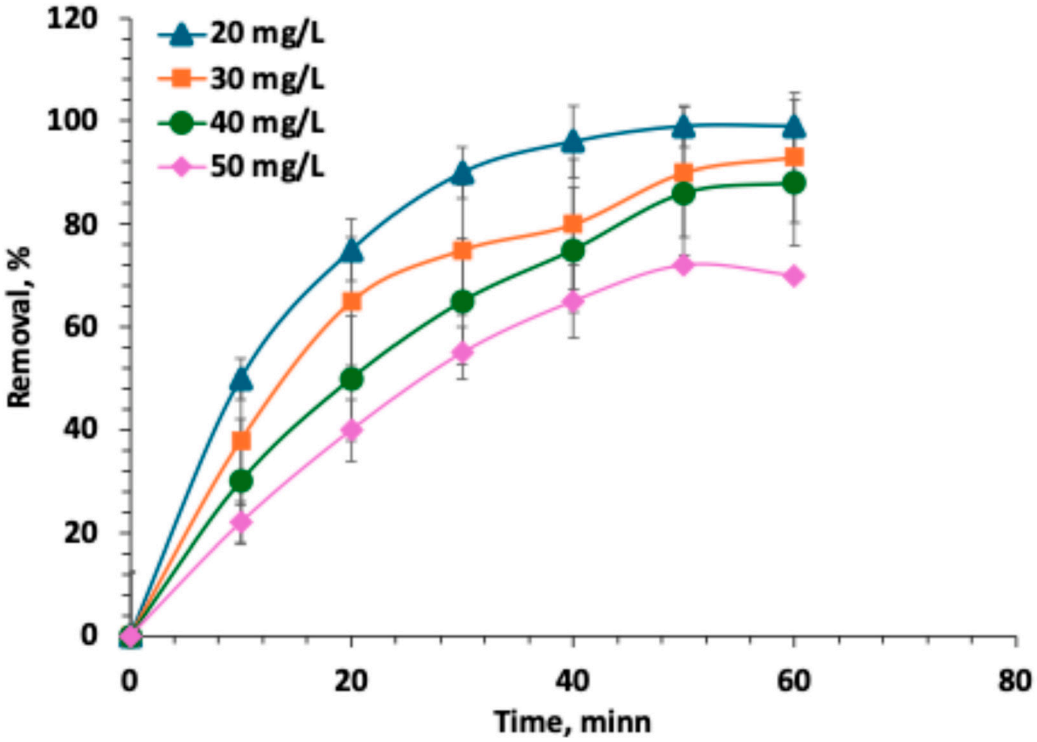


Figure 10. Effect of initial Red SPR dye concentration on the solar photo-Fenton degradation efficiency using MIL-100(Fe) under fixed operating conditions (pH 3.0, H_2O_2 = 400 mg L^{-1}, Fe = 40 mg L^{-1}).

In addition, higher dye concentrations increase competition between pollutant molecules and intermediate species for the available reactive oxygen species (ROS), resulting in insufficient radical availability per molecule. For example, while 20 mg L^{-1} achieved ~90% removal within 40 min, the 50 mg L^{-1} system reached only ~65% under the same conditions, confirming the reduced oxidation efficiency at higher loadings. Furthermore, accumulation of intermediate degradation products at elevated concentrations may contribute to radical scavenging, further inhibiting the process. Conversely, at lower dye concentrations, the ratio of ROS to pollutant molecules is higher, enabling more effective radical attack, enhanced catalytic turnover, and improved mineralization pathways. The active sites of the MIL-100(Fe) catalyst also remain more accessible, contributing to improved performance. Therefore, it is noteworthy to mention that such results confirm that initial dye concentration is a critical operational parameter, and maintaining lower pollutant loadings significantly enhances the efficiency of the solar photo-Fenton process. This investigation is in agreement with previous studies [28,50] which reported similar decreases in degradation efficiency with increasing organic load due to light screening and radical competition effects. Recent investigations on Fe-based MOFs, including MIL-

100(Fe), further confirm that optimal photocatalytic performance is achieved at lower contaminant concentrations, where photon utilization and ROS generation are maximized.

2.6.7. Effect of Temperature

Figure 11 shows that temperature has a pronounced effect on the degradation kinetics of Red SPR dye. Increasing the temperature from 25 to 55 °C significantly accelerates the reaction rate, particularly during the initial stages of the process. For instance, the removal efficiency at 10 min increases from approximately 60% at 25 °C to 88% at 55 °C, indicating enhanced reaction kinetics at elevated temperatures. This improvement can be attributed to the increased rate of H_2O_2 decomposition and enhanced generation of hydroxyl radicals (•OH), as well as improved mass transfer and molecular interactions at higher temperatures. Additionally, elevated temperatures promote faster Fe^{3+}/Fe^{2+} redox cycling within the MIL-100(Fe) framework, further enhancing catalytic activity.

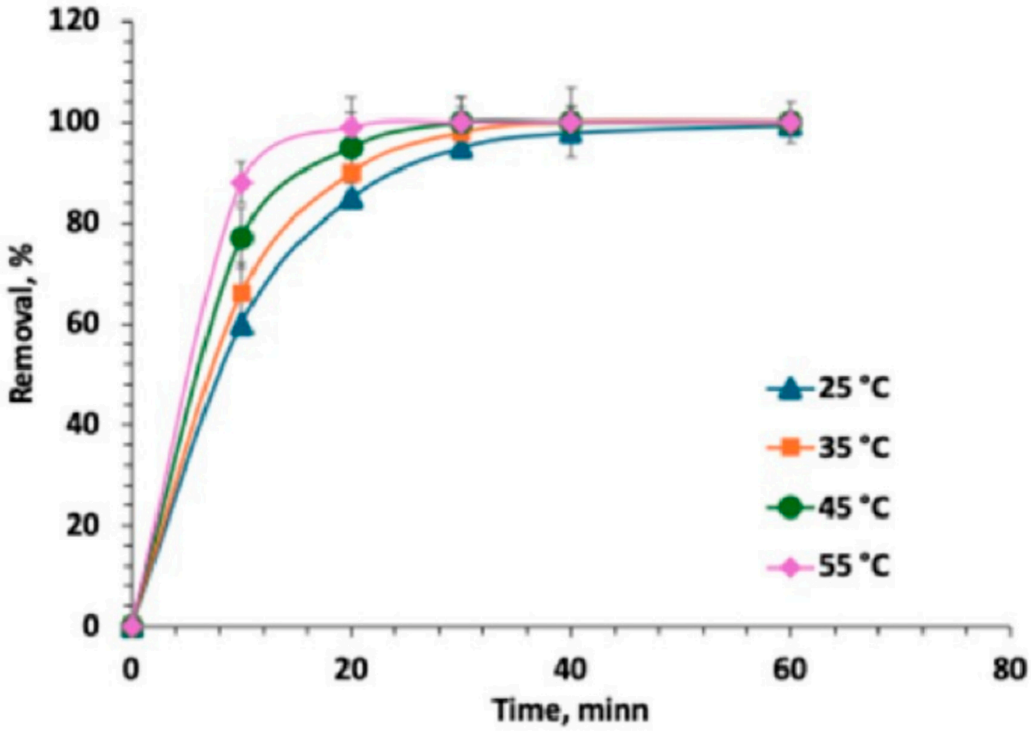


Figure 11. Effect of reaction temperature on the solar photo-Fenton degradation of Red SPR dye using MIL-100(Fe) under fixed operating conditions (pH 3.0, H_2O_2 = 400 mg L^{-1}, MOF = 40 mg L^{-1}, initial dye concentration = 20 mg L^{-1}).

However, despite the significant differences in initial degradation rates, all temperature conditions ultimately achieve near-complete removal—almost 100%—within 40–60 min, indicating that temperature primarily influences the reaction rate rather than the final degradation efficiency. This suggests that the system is not limited by thermodynamics but rather by reaction kinetics. From a practical perspective, although higher temperatures (55 °C) provide faster degradation, the marginal benefit in final removal does not justify the additional energy input required for heating. Therefore, operating at moderate temperatures (35–45 °C) offers an optimal balance between reaction efficiency and energy consumption. These results are in accordance with previous studies [50,51] on photo-Fenton systems, where increasing temperature enhances reaction kinetics but does not significantly alter the ultimate removal efficiency due to the high oxidative capacity of hydroxyl radicals. Hence, although the elevated temperatures accelerate degradation kinetics, the negligible

difference in final removal efficiency confirms that moderate temperature conditions are sufficient and more energy-efficient for practical applications [50].

2.6.8. Radical Scavenger Test

To elucidate the dominant reactive oxygen species involved in the degradation process, radical scavenger experiments were conducted under optimized conditions, as illustrated in Figure 12. The data displayed in Figure 12 presents the effect of different radical scavengers on the degradation efficiency of Red SPR dye, providing insight into the primary reactive oxygen species (ROS) responsible for the oxidation process in the MIL-100(Fe)-based solar photo-Fenton system. In the absence of scavengers, the system exhibits nearly complete degradation (about 100%) within the reaction time, confirming the high efficiency of the catalytic process. Upon the addition of tert-butanol (TBA), a well-known hydroxyl radical (•OH) scavenger, a significant decrease in degradation efficiency is observed. This clearly indicates that •OH radicals are the dominant oxidizing species responsible for dye degradation. Similarly, the introduction of p-benzoquinone (BQ), a scavenger for superoxide radicals (O_2•$^-$), results in a moderate reduction in degradation efficiency, suggesting that superoxide radicals also contribute to the oxidation process, although to a lesser extent than •OH. However, the addition of ammonium oxalate (AO) or EDTA, which act as hole (h^+) scavengers, leads to a slight decrease in removal efficiency, indicating a minor contribution of photogenerated holes in the overall mechanism [28,49].

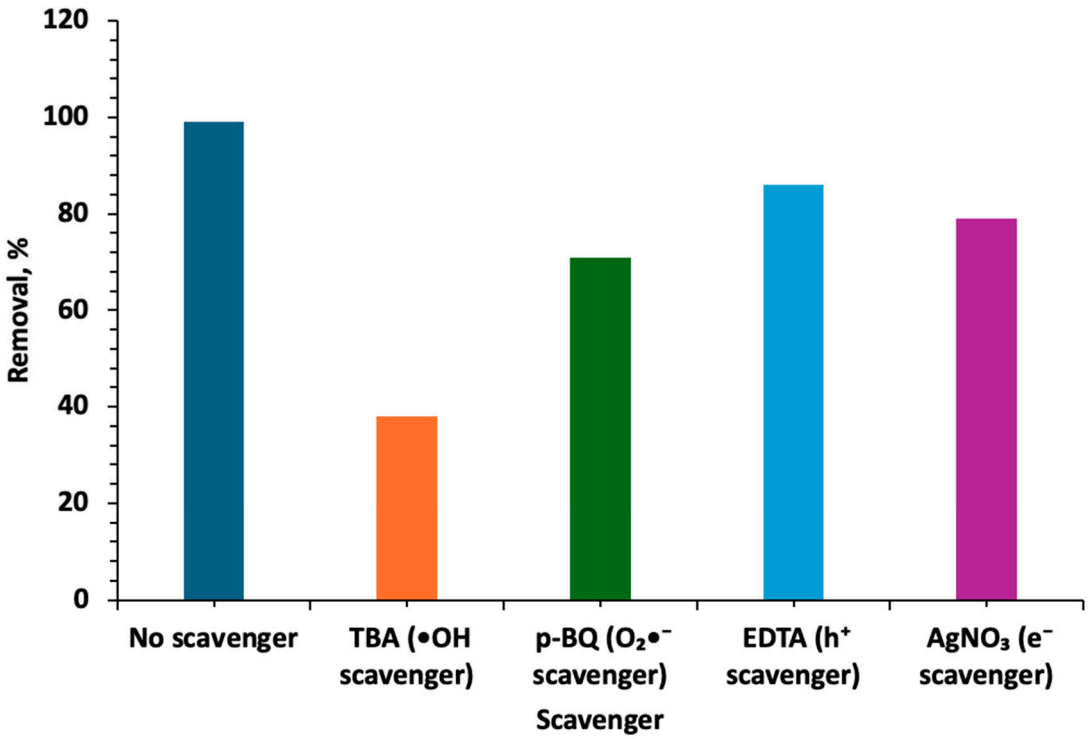


Figure 12. Effect of different radical scavengers on the degradation efficiency of Red SPR dye during the solar photo-Fenton process over MIL-100(Fe) under optimized operating conditions (pH 3.0, H_2O_2 = 400 mg L^{-1}, MOF = 40 mg L^{-1}, initial dye concentration = 20 mg L^{-1}).

The pronounced inhibition observed in the presence of TBA confirms that the degradation mechanism is predominantly governed by hydroxyl radicals generated via the Fenton and photo-Fenton reactions. The partial suppression observed with BQ further suggests a secondary role of superoxide radicals, likely formed through the reduction of dissolved oxygen or H_2O_2 photolysis pathways. These results are consistent with previous studies on Fe-based MOF systems, including MIL-100(Fe), where •OH radicals are identified as

the primary reactive species, with additional contributions from $O_2\bullet^-$ and other ROS depending on reaction conditions. The radical scavenger experiments confirm that the degradation of Red SPR dye is predominantly governed by hydroxyl radicals (•OH), with additional but less significant contributions from superoxide radicals ($O_2\bullet^-$), supporting the proposed solar photo-Fenton mechanism over MIL-100(Fe) [52,53].

2.6.9. Iron Leaching, Catalyst Recovery, and Heterogeneity

To evaluate the heterogeneous nature, recovery behavior, and structural stability of the MIL-100(Fe)-based solar photo-Fenton system, iron leaching analysis and catalyst-removal experiments were conducted under the optimized operating conditions. The iron leaching analysis revealed a dissolved Fe concentration of 1.2 mg L^{-1} after the reaction, corresponding to approximately 3.0 wt% relative to the initially applied MIL-100(Fe) catalyst dosage (40 mg L^{-1}), indicating limited iron release during the oxidation process.

After completion of the reaction, the MIL-100(Fe) catalyst was successfully recovered from the treated solution by filtration, followed by repeated washing with distilled water and ethanol to remove residual intermediates and adsorbed species. The recovered catalyst was then dried prior to reuse, demonstrating the practical recoverability of the heterogeneous catalyst system.

Furthermore, the catalyst-removal experiment demonstrated that after separating the MIL-100(Fe) catalyst from the reaction suspension, only negligible additional dye degradation occurred. This observation confirms that the oxidation process was predominantly governed by heterogeneous surface-mediated catalysis rather than homogeneous dissolved Fe species. Compared with conventional homogeneous Fenton systems based on dissolved Fe^{2+} ions, the heterogeneous MIL-100(Fe)-based system offers additional advantages, including reduced ferric sludge generation, easier catalyst separation, and minimized secondary pollution. These findings confirm the good structural stability and heterogeneous catalytic behavior of MIL-100(Fe) under the investigated solar photo-Fenton conditions.

2.7. 100(Fe) Hydroxyl Radical Generation and Reaction Mechanism

The catalytic mechanism of the solar-assisted photo-Fenton-like process over MIL-100(Fe) is governed by the continuous generation of highly reactive oxygen species (ROS), primarily hydroxyl radicals (•OH), through iron redox cycling and light irradiation. The overall mechanism is schematically illustrated in Figure 13, while the fundamental reaction pathways responsible for ROS generation and dye degradation are summarized in Equations (1)–(15).

As shown in Figure 13, MIL-100(Fe) acts as a heterogeneous catalyst in which Fe^{3+} active sites embedded within the porous framework undergo continuous redox cycling. Initially, Fe^{2+} reacts with hydrogen peroxide (H_2O_2) to generate •OH radicals and Fe^{3+} via the classical Fenton reaction (Equation (1)). The produced Fe^{3+} is subsequently reduced back to Fe^{2+} through reaction with hydroperoxyl radicals ($HO_2\bullet$) (Equation (2)) and via interaction with H_2O_2 (Equation (4)), thereby sustaining the catalytic cycle. Simultaneously, H_2O_2 participates in several secondary reactions that contribute to the formation of additional ROS. In particular, •OH reacts with H_2O_2 to produce superoxide radicals ($O_2\bullet^-$) and $HO_2\bullet$ (Equations (3) and (5)). These reactions play a crucial role in maintaining a dynamic equilibrium among different reactive species in the system. However, some reactions may act as radical scavenging or recombination pathways. For example, •OH can be consumed through reaction with Fe^{2+} (Equation (6)), while radical recombination processes such as •OH self-quenching (Equation (7)) and $HO_2\bullet$ disproportionation (Equation (8)) reduce the overall availability of active oxidants. Additional side reactions, including the interaction of Fe^{2+} with $HO_2\bullet$ (Equation (9)) and the reaction between H_2O_2 and $HO_2\bullet$ (Equation (10)),

further influence the balance of ROS in the system. Under solar irradiation, the catalytic process is significantly enhanced through photo-Fenton reactions. As described in Equation (11), Fe^{2+} reacts with H_2O_2 under light irradiation to produce additional •OH radicals. Furthermore, $Fe(OH)^{2+}$ species undergo photoreduction to regenerate Fe^{2+} (Equation (12)), while direct photolysis of H_2O_2 yields two •OH radicals (Equation (13)). These photochemical pathways greatly accelerate ROS generation and improve the overall reaction kinetics [26].

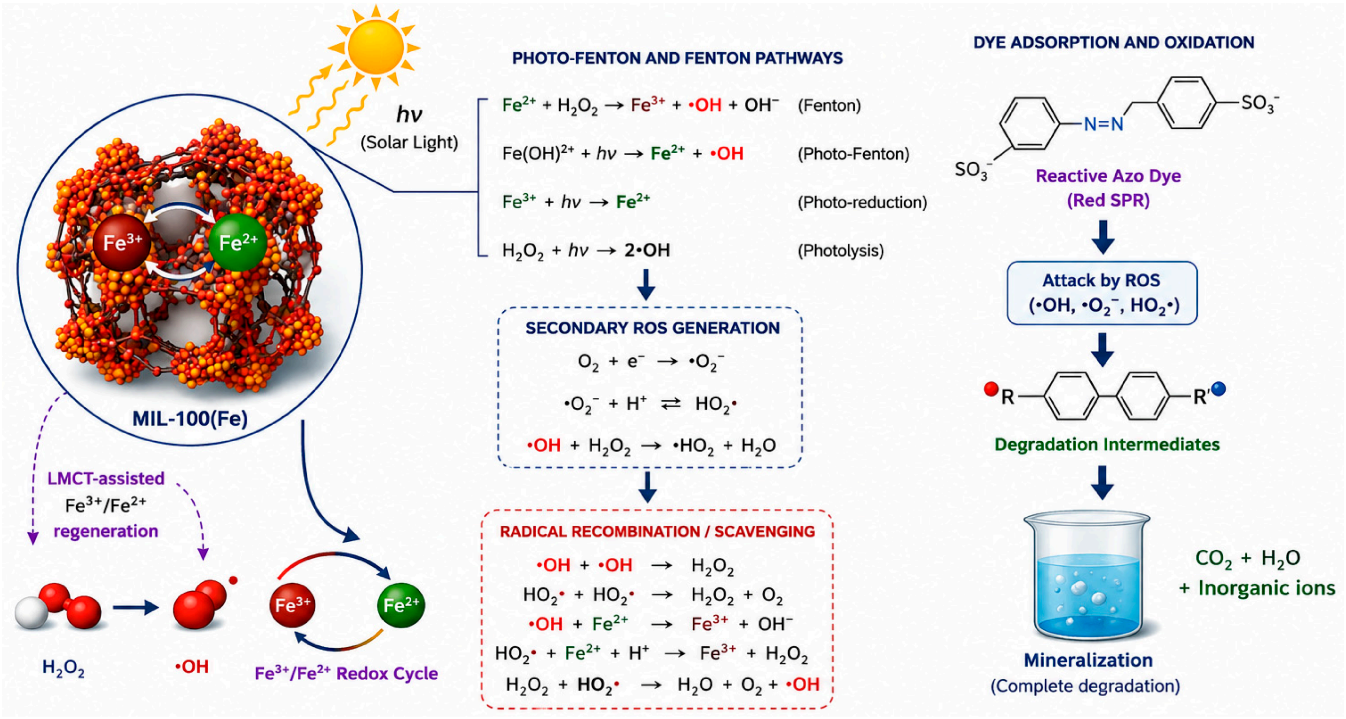


Figure 13. Schematic illustration of mechanistic pathway of reactive azo dye degradation via solar-activated MIL-100(Fe)/H_2O_2 system.

In addition, the unique structure of MIL-100(Fe) enables ligand-to-metal charge transfer (LMCT), as described in Equation (15), where Fe^{3+} complexes are photoreduced to Fe^{2+} with the simultaneous formation of ligand-centered radicals (L•). This process further enhances Fe^{2+} regeneration and promotes sustained catalytic activity. Here, L represents the organic ligand within the MIL-100(Fe) framework. The generated ROS, particularly •OH and O_2•$^-$, are highly oxidative and non-selectively attack the azo (–N=N–) bonds and aromatic structures of dye molecules, leading to their fragmentation into intermediate compounds (Equation (14)). These intermediates are subsequently oxidized through successive reactions until complete mineralization into CO_2, H_2O, and inorganic ions is achieved. Overall, the coupled Fenton, photo-Fenton, and LMCT processes demonstrate the synergistic role of solar irradiation and the Fe^{3+}/Fe^{2+} redox cycle in enhancing ROS generation and improving the photocatalytic degradation efficiency of the MIL-100(Fe)/H_2O_2 system. Additionally, as illustrated in Figure 13, the mesoporous structure of MIL-100(Fe) facilitates mass transfer and provides abundant accessible active sites, further contributing to the enhanced catalytic performance [54].

The proposed mechanism was further clarified to distinguish between the primary ROS generation pathways and the secondary radical transformation/recombination reactions occurring within the MIL-100(Fe)/H_2O_2 system. Hydroxyl radicals (•OH) were identified as the dominant oxidative species responsible for Red SPR dye degradation, whereas O_2•$^-$ and HO_2• mainly participate in secondary redox reactions and Fe^{3+}/Fe^{2+}

regeneration pathways. In addition, solar irradiation enhances the catalytic process through Fe^{3+} photoreduction, accelerated H_2O_2 photolysis, and improved Fe^{2+} regeneration via photo-Fenton and ligand-to-metal charge transfer (LMCT) processes. Moreover, the porous MIL-100(Fe) framework facilitates reactant diffusion and provides abundant accessible active sites, thereby promoting ROS generation and enhancing the overall heterogeneous solar photo-Fenton degradation efficiency.

$$Fe^{2+} + H_2O_2 \rightarrow Fe^{3+} + OH^- + OH^{\cdot} \quad (1)$$

$$Fe^{3+} + OH_2^{\cdot} \rightarrow Fe^{2+} + O_2 + H^+ \quad (2)$$

$$H_2O_2 + HO^{\cdot} \rightarrow H^+ + O_2^{\cdot} + H_2O \quad (3)$$

$$Fe^{3+} + H_2O_2 \rightarrow Fe^{2+} + OH_2^{\cdot} + H^+ \quad (4)$$

$$H_2O_2 + HO^{\cdot} \rightarrow HO_2^{\cdot} + H_2O \quad (5)$$

$$Fe^{2+} + OH^{\cdot} \rightarrow Fe^{3+} + OH^- \quad (6)$$

$$OH^{\cdot} + OH^{\cdot} \rightarrow H_2O_2 \quad (7)$$

$$2OH_2^{\cdot} \rightarrow H_2O_2 + O_2 \quad (8)$$

$$Fe^{2+} + OH_2^{\cdot} + H^+ \rightarrow Fe^{3+} + H_2O_2 \quad (9)$$

$$H_2O_2 + HO_2^{\cdot} \rightarrow H_2O + O_2 + HO^{\cdot} \quad (10)$$

$$Fe^{2+} + H_2O_2 + h\nu \rightarrow Fe^{3+} + OH^- + OH^{\cdot} \quad (11)$$

$$Fe(OH)^{2+} + h\nu \rightarrow Fe^{2+} + H^+ \ (\lambda < 580\ \text{nm}) \quad (12)$$

$$H_2O_2 + h\nu \rightarrow 2OH^{\cdot} \ (\lambda < 310\ \text{nm}) \quad (13)$$

$OH^{\cdot}$ +  ↔  → Reaction intermediates → *Further oxidation reactions* (14)

$$Fe^{3+}L_n + h\nu \rightarrow Fe^{2+}L_{n-1} + L^{\cdot} \quad (15)$$

Overall, the synergistic interaction between solar irradiation and the Fe^{3+}/Fe^{2+} redox cycle significantly enhances the photocatalytic degradation efficiency of the MIL-100(Fe)/H_2O_2 system.

2.8. Kinetics and Thermodynamic Analysis

To gain deeper insight into the degradation mechanism of Red SPR dye over MIL-100(Fe), the experimental data obtained at different temperatures were analyzed using kinetic and thermodynamic models. The kinetic parameters presented in Table 1 clearly demonstrate the strong influence of temperature on the degradation rate of reactive Red SPR dye in the MIL-100(Fe)-based solar photo-Fenton system. For the pseudo-first-order model, the rate constant (k_1) increased from 0.1040 min^{-1} at 25 °C to 0.1589 min^{-1} at 55 °C, indicating a significant enhancement in reaction kinetics with increasing temperature. Correspondingly, the half-life time ($t_{1/2}$) decreased from 6.66 min to 4.36 min, confirming that higher temperatures accelerate the degradation process. The high correlation coefficients (R^2 = 0.98–0.99) obtained for the pseudo-first-order model indicate an excellent fit to the experimental data, suggesting that the degradation process is well described by this kinetic model. This behavior is typical of photo-Fenton systems, where the reaction rate is primar-

ily governed by the concentration of the pollutant and the availability of reactive oxygen species (ROS), particularly hydroxyl radicals (•OH) [5,28].

Table 1. Parameters of first- and second-kinetic models for reactive Red SPR dye removals through solar photo-Fenton system.

Linearized Kinetic Model	Kinetic Variables	Temperature, °C			
		25 °C	**35 °C**	**45 °C**	**55 °C**
Pseudo-first-order ($C_t = C_o - e^{k_1 t}$)	k_1 (min^{-1})	0.1040	0.1417	0.1568	0.1589
	$t_{1/2}$ (min)	6.66	4.89	4.42	4.36
	R^2	0.99	0.98	0.99	0.99
Pseudo-second-order ($\left(\frac{1}{C_t}\right) = \left(\frac{1}{C_0}\right) - k_2 t$)	k_2 ($L.mg^{-1}.min^{-1}$)	0.0438	0.1176	0.2391	0.4792
	$t_{1/2}$ (min)	0.9162	0.8461	0.8689	0.9038
	R^2	0.91	0.84	0.86	0.90

In contrast, although the pseudo-second-order rate constant (k_2) also increased with temperature (from 0.0438 to 0.4792 L mg^{-1} min^{-1}), the corresponding R^2 values (0.84–0.91) were consistently lower than those of the pseudo-first-order model. This indicates a poorer fit and suggests that the second-order model is less suitable for describing the degradation kinetics of Red SPR dye under the studied conditions. Moreover, the half-life values derived from the pseudo-second-order model showed less consistent trends, further supporting this conclusion. Hence, the results confirm that the degradation of Red SPR dye over MIL-100(Fe) follows pseudo-first-order kinetics, with the reaction rate significantly enhanced at elevated temperatures. This behavior can be attributed to the increased generation of hydroxyl radicals, improved mass transfer, and accelerated Fe^{3+}/Fe^{2+} redox cycling within the MIL-100(Fe) framework. These findings indicate that the degradation process is predominantly governed by radical-mediated oxidation mechanisms, with temperature playing a key role in enhancing the reaction kinetics rather than altering the fundamental reaction pathway.

The thermodynamic parameters, including Gibbs free energy (ΔG‘), enthalpy (ΔH‘), and entropy (ΔS‘) of activation, were calculated from the temperature-dependent kinetic data. Table 2 summarizes these parameters, providing insights into the energetic aspects of the Red SPR dye degradation process under the MIL-100(Fe)-based solar photo-Fenton system.

Table 2. Thermodynamic parameters for reactive Red SPR dye oxidation over the MIL-100(Fe)-based solar photo-Fenton system.

Thermodynamic Parameters	T/°C			
	25 °C	**40 °C**	**50 °C**	**60 °C**
ΔG‘ (kJ/mol)	78.45	80.79	83.13	85.47
ΔH‘ (kJ/mol)	8.72	8.72	8.72	8.72
ΔS‘ (J/mol K)	−233.88	−233.88	−233.88	−233.88
Ea (kJ/mol)	11.32			

The calculated thermodynamic parameters indicate that the degradation of reactive Red SPR dye over MIL-100(Fe) is a thermally assisted process with a relatively low activation energy (E_a = 11.32 kJ mol^{-1}), confirming that the oxidation proceeds readily under the investigated conditions. The positive value of ΔH‘ (8.72 kJ mol^{-1}) suggests that the activation step is endothermic in nature. In contrast, the negative ΔS‘ value (−233.88 J mol^{-1} K^{-1}) indicates the formation of a more ordered activated complex during the degradation

process. The positive $\Delta G'$ values, which increase with temperature, reflect the existence of an activation barrier for the reaction step. Nevertheless, the low E_a value and the rapid experimental degradation confirm that the solar photo-Fenton oxidation of Red SPR dye over MIL-100(Fe) is kinetically favorable and efficiently promoted by increasing temperature. Hence, the thermodynamic results support the kinetic findings and confirm that Red SPR dye degradation over MIL-100(Fe) is an energetically feasible, temperature-enhanced oxidation process.

It is noteworthy to mention that the relatively low activation energy value obtained in the present study (Ea = 11.32 kJ mol^{-1}) indicates that the degradation process proceeds readily once reactive oxygen species are generated, which is characteristic of radical-mediated photo-Fenton oxidation systems. In heterogeneous solar photo-Fenton processes, the apparent activation energy reflects the combined contribution of several coupled phenomena, including H_2O_2 decomposition, Fe^{3+}/Fe^{2+} redox cycling, hydroxyl radical generation, adsorption–desorption interactions, and mass-transfer effects, rather than representing only the intrinsic surface reaction barrier [55,56].

Therefore, although the calculated Ea value is relatively low, increasing the reaction temperature still significantly enhances the initial degradation kinetics by accelerating H_2O_2 activation, improving Fe^{2+} regeneration, increasing molecular diffusion, and promoting more effective interaction between dye molecules and reactive oxygen species. Consequently, the pronounced increase in early-stage degradation efficiency observed at elevated temperatures mainly reflects enhanced radical generation and faster reaction kinetics rather than a contradiction with the relatively low activation energy value.

2.9. Limitations and Future Perspectives

Although the MIL-100(Fe)-based solar photo-Fenton system demonstrated high degradation efficiency toward reactive azo dye (Red SPR), several limitations should be considered. The current investigation was performed using a synthetic dye solution under controlled laboratory conditions, which may not fully represent the complexity of real textile wastewater containing competing organic compounds, inorganic ions, surfactants, and suspended solids that could influence catalyst performance and reactive oxygen species generation. In addition, the experiments were conducted under natural solar irradiation, where fluctuations in solar intensity and environmental conditions may affect process reproducibility and large-scale operational stability under practical outdoor applications.

Furthermore, while the synthesized MIL-100(Fe) exhibited efficient catalytic activity, additional investigations concerning long-term catalyst durability, continuous-flow large-scale operation, and extended stability under repeated solar photo-Fenton cycles are still necessary before practical industrial implementation. Future studies should therefore focus on real textile wastewater treatment, pilot-scale reactor evaluation, catalyst lifetime assessment, and process optimization under variable environmental conditions to further validate the practical applicability of the developed solar-assisted heterogeneous photo-Fenton system.

3. Experimental Investigation

3.1. Synthesis of MIL-100(Fe)

Iron(III) nitrate nonahydrate ($Fe(NO_3)_3 \cdot 9H_2O$, ≥98%) and benzene-1,3,5-tricarboxylic acid (H_3BTC, ≥95%) were purchased from Sigma-Aldrich. N,N-dimethylformamide (DMF, ≥99.8%) and ethanol (≥99.9%) were obtained from Merck. Distilled water (Merck KGaA, Darmstadt, Germany) was used throughout all washing steps. All chemicals were of analytical grade and used without further purification. MIL-100(Fe) was synthesized via a solvothermal method. Briefly, $Fe(NO_3)_3 \cdot 9H_2O$ (2 mmol) and H_3BTC (1 mmol) were

dissolved in 30 mL DMF under continuous magnetic stirring at room temperature for 30 min to obtain a homogeneous solution. The mixture was then transferred into a Teflon-lined stainless-steel autoclave and heated at 100 °C for 24 h. After naturally cooling to room temperature, the resulting solid product was collected by centrifugation and washed with distilled water and ethanol (three times each) to remove unreacted precursors and residual solvent. The product was then dried at 75 °C. Finally, the dried material was thermally activated at 150 °C for 24 h to remove trapped solvent molecules and obtain the activated MIL-100(Fe).

3.2. Preparation of Synthetic Dye Solution

A commercially available reactive azo dye, Red SPR (trade name, Kisco International, Adana, Turkey), was selected as a model organic contaminant to evaluate the catalytic performance of the synthesized MIL-100(Fe) in Fenton and photo-Fenton processes. The use of a model dye enables controlled investigation of degradation efficiency and reaction mechanisms relevant to textile wastewater treatment.

A synthetic aqueous solution was prepared to simulate dye-containing effluents under well-defined laboratory conditions. A stock solution (1000 $mg \cdot L^{-1}$) was obtained by dissolving an accurately weighed amount of Red SPR powder in distilled water, followed by thorough mixing to ensure complete dissolution. Working solutions of the desired concentrations were then prepared by serial dilution of the stock solution.

This approach provides a reproducible system for systematically assessing catalytic activity, reaction kinetics, and degradation pathways of the MIL-100(Fe) catalyst, while minimizing matrix interferences typically present in real wastewater. Consequently, it allows clearer interpretation of the role of active Fe sites and reactive oxygen species in the degradation process.

3.3. Solar Photo-Fenton Experimental Setup and Procedure

The solar photo-Fenton experiments were conducted using a parabolic trough solar collector system integrated with a tubular reactor and a circulation tank. The experimental setup consisted of a transparent tubular reactor mounted over a flat plate collector to maximize solar irradiation exposure. The reactor was connected to a storage tank through a continuous circulation loop using a peristaltic pump, ensuring uniform mixing and consistent contact between the catalyst, oxidant, and dye solution. Then, a known volume of the reactive azo dye solution (Red SPR) with a predetermined concentration was introduced into the tank, followed by the addition of a specific dosage of the MIL-100(Fe) catalyst and hydrogen peroxide (H_2O_2). The initial pH of the solution was adjusted to the desired value using dilute sulfuric acid (H_2SO_4, 0.1–1.0 M) or sodium hydroxide (NaOH, 0.1–1.0 M), prepared from analytical-grade reagents (≥98%, Sigma-Aldrich, Darmstadt, Germany) using distilled water. The suspension was circulated continuously between the tank and the tubular reactor at a constant flow rate under natural solar irradiation.

Prior to irradiation, the reaction mixture was stirred in the dark for a certain period to establish adsorption–desorption equilibrium between the dye molecules and the catalyst surface. Upon exposure to sunlight, the photo-Fenton reaction was initiated, and the degradation process was monitored over time. All experiments were carried out during the summer season under natural sunlight to ensure high and stable solar irradiance. The ambient temperature and solar intensity were recorded throughout the experimental period to maintain consistency and reproducibility.

Samples were withdrawn from the system at regular time intervals of 10 min. Each sample was immediately centrifuged to remove catalyst particles and analyzed using UV–Vis spectrophotometry at λmax = 505 nm to determine the residual dye concentration. The

degradation efficiency was calculated based on the change in concentration over time. The experimental setup of the solar photo-Fenton system, incorporating a parabolic trough collector coupled with a tubular quartz reactor and a recirculation loop, is illustrated in Figure 14.

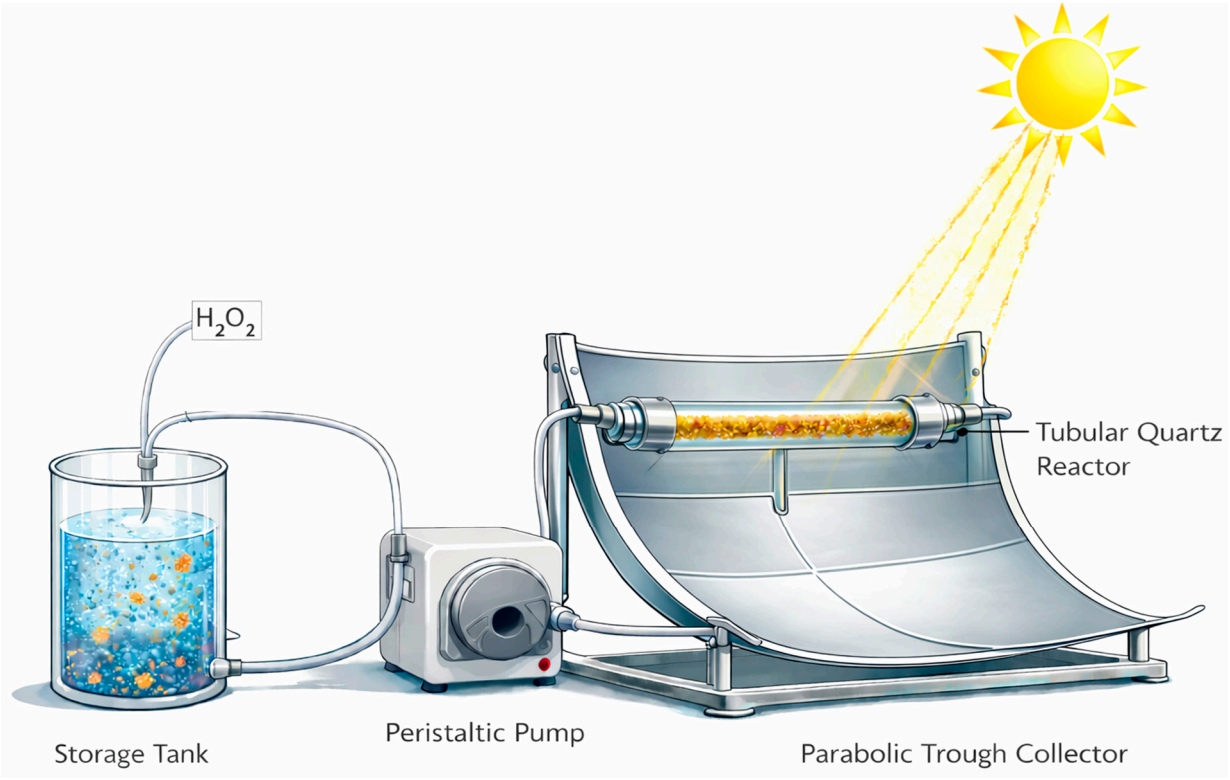


Figure 14. Schematic representation of the solar photo-Fenton experimental setup using a parabolic trough collector.

The solar irradiance during the experimental runs was continuously monitored using an ISO 9060 (Kipp & Zonen, Delft, The Netherlands) second-class pyranometer from Kipp & Zonen®, Delftechpark, The Netherlands (Model CMP3) during the solar illumination period. The measured solar intensity during the experiments ranged approximately from 650 to 920 W m^{-2} under clear daytime conditions. All experiments were conducted during the summer season within a fixed daytime interval under relatively stable weather conditions to minimize fluctuations in solar irradiation. In addition, ambient temperature and solar intensity were continuously recorded throughout the experiments to maintain consistency and improve the reproducibility of the solar-assisted oxidation process.

To identify the dominant reactive oxygen species involved in the solar photo-Fenton degradation mechanism, radical scavenger experiments were conducted under the optimized operating conditions (pH 3.0, H_2O_2 = 400 mg L^{-1}, MIL-100(Fe) = 40 mg L^{-1}, and initial Red SPR dye concentration = 20 mg L^{-1}). Prior to solar irradiation, the reaction mixture was stirred in the dark for 20 min to establish adsorption–desorption equilibrium. Different scavengers were individually added to the reaction system before irradiation, including tert-butanol (TBA) as a hydroxyl radical (•OH) scavenger, p-benzoquinone (BQ) as a superoxide radical (O_2•$^-$) scavenger, and ammonium oxalate (AO) as a photogenerated hole (h^+) scavenger. The concentration of each scavenger was maintained throughout the experiments. The degradation efficiency of Red SPR dye was monitored under natural solar irradiation using UV–Vis spectrophotometry at λmax, and the obtained results were used to evaluate the contribution of the different reactive species to the oxidation process.

3.4. Analytical Technique

The concentration of the reactive azo dye was determined using UV–Vis spectrophotometry (UNICO UV-2100 spectrophotometer, North Charleston, South Carolina). Absorption spectra were recorded over the wavelength range of 200–800 nm, and the maximum absorbance (λmax) of the dye was identified at 505 nm. This characteristic wavelength was used to monitor the degradation process during the catalytic oxidation experiments. At predetermined time intervals, aliquots were withdrawn from the reaction mixture and, when necessary, centrifuged to remove suspended catalyst particles prior to analysis. The residual dye concentration was calculated from the absorbance at 505 nm using a previously established calibration curve based on the Beer–Lambert law.

3.5. Characterization

The physicochemical properties and structural characteristics of the synthesized MIL-100(Fe) were systematically investigated using a set of analytical techniques consistent with previously reported methodologies. X-ray diffraction (XRD) patterns were recorded using a Bruker D8 (Zurich, Switzerland) Advance X-ray diffractometer equipped with Cu Kα radiation (λ = 1.5406 Å), where data were collected over a 2θ range of 5–50° at a scanning rate of 2° min^{-1} to assess the crystallinity and phase purity of the synthesized material. To further examine the surface morphology and microstructural features, Scanning Electron Microscopy (SEM) analysis was performed using a JEOL JSM-6510LV, with samples sputter-coated with a thin gold layer prior to imaging to enhance conductivity and improve resolution. In conjunction with SEM, energy-dispersive x-ray spectroscopy (EDX) was carried out using an Oxford Instruments X-Max EDX detector to determine the elemental composition and distribution, with measurements conducted at an accelerating voltage of 15–20 kV to enable clear detection of Fe, O, and C elements. Additionally, Fourier Transform Infrared Spectroscopy (FTIR) measurements were performed using a (Unico 2100 FTIR, North Charleston, South Carolina) spectrophotometer in the wavenumber range of 4000–400 cm^{-1}, where samples prepared via the KBr pellet method were analyzed to identify functional groups and confirm the coordination between iron centers and the organic ligand.

4. Conclusions

In this work, MIL-100(Fe) was successfully synthesized and applied as an effective heterogeneous catalyst for the solar-assisted photo-Fenton degradation of reactive Red SPR dye. The system exhibited high catalytic efficiency, achieving nearly complete dye removal under optimized conditions (pH 3.0, H_2O_2 = 400 mg L^{-1}, MOF = 40 mg L^{-1}). The degradation process was well described by pseudo-first-order kinetics, with reaction rates increasing with temperature, confirming the thermally enhanced nature of the process. Thermodynamic analysis revealed that the reaction is endothermic and kinetically favorable, while radical scavenger experiments demonstrated that hydroxyl radicals (•OH) are the primary reactive species responsible for dye oxidation. The enhanced performance is attributed to the synergistic effect of solar irradiation and the Fe^{3+}/Fe^{2+} redox cycle within the MIL-100(Fe) framework. Thus, the findings highlight the strong potential of MIL-100(Fe)-based solar photo-Fenton systems as efficient, sustainable, and economically viable solutions for the treatment of dye-contaminated wastewater.

Author Contributions: Conceptualization, M.A.T.; Methodology, M.A.T.; Software, M.M.N. and H.A.N.; Validation, M.M.N. and H.A.N.; Resources, M.M.N.; Data curation, H.A.N. and M.A.T.; Writing—original draft, M.M.N., H.A.N. and M.A.T.; Writing—review & editing, M.M.N., H.A.N. and M.A.T.; Visualization, M.M.N. and H.A.N. All authors have read and agreed to the published version of the manuscript.

Funding: This research was funded by Prince Sattam bin Abdulaziz University-(PSAU/2026/03/43604).

Data Availability Statement: Data are available upon request.

Acknowledgments: The authors extend their appreciation to Prince Sattam bin Abdulaziz University for funding this research work through the project number (PSAU/2026/03/43604).

Conflicts of Interest: The authors declare no conflicts of interest.

References

1. Periyasamy, A.P. Textile Dyes in Wastewater and its Impact on Human and Environment: Focus on Bioremediation. *Water Air Soil Pollut.* **2025**, *236*, 562. [CrossRef]
2. Kumari, U. Textile dyes and their impact on the natural environment. In *Dye Pollution from Textile Industry: Challenges and Opportunities for Sustainable Development*; Springer: Berlin/Heidelberg, Germany, 2024; pp. 17–30.
3. Awad, M.E.; Farrag, A.M.; Aboelnga, M.M.; El-Bindary, A.A. Optimization of Photocatalytic Degradation of Rhodamine B and Indigo Carmine Dyes Using Eco-Friendly Kaolinite-Silver Oxide Quantum Dots Nanocomposite Under Sunlight Irradiation. *Appl. Organomet. Chem.* **2025**, *39*, e7842. [CrossRef]
4. Ogwu, M.C.; Pamela, B.O.; Dare, A.F.; Ovuru, K.F.; Iyiola, A.O. Traditional and conventional water treatment methods: A sustainable approach. In *Water Crises and Sustainable Management in the Global South*; Springer: Berlin/Heidelberg, Germany, 2024; pp. 461–486.
5. Quang, H.H.P.; Dinh, N.T.; Thi, T.N.T.; Bao, L.T.N.; Yuvakkumar, R.; Nguyen, V.-H. Fe^{2+}, Fe^{3+}, Co^{2+} as highly efficient cocatalysts in the homogeneous electro-Fenton process for enhanced treatment of real pharmaceutical wastewater. *J. Water Process Eng.* **2022**, *46*, 102635. [CrossRef]
6. Senkovska, I.; Bon, V.; Mosberger, A.; Wang, Y.; Kaskel, S. Adsorption and Separation by Flexible MOFs. *Adv. Mater.* **2025**, *37*, e2414724. [CrossRef]
7. Feng, W.; Deng, Y.; Yang, F.; Miao, Q.; Ngien, S.K. Systematic Review of Contaminants of Emerging Concern (CECs): Distribution, Risks, and Implications for Water Quality and Health. *Water* **2023**, *15*, 3922. [CrossRef]
8. Lapworth, D.J.; Baran, N.; Stuart, M.E.; Ward, R.S. Emerging organic contaminants in groundwater: A review of sources, fate and occurrence. *Environ. Pollut.* **2012**, *163*, 287–303. [CrossRef]
9. Sellaoui, L.; Edi-Soetaredjo, F.; Mohamed, M.; Ismadji, S.; Ernst, B.; Bonilla-Petriciolet, A.; Lamine, A.B.; Dell, D.; Badawi, M. A novel application of HKUST-1 for textile dyes removal in single and binary solutions: Experimental investigation combined with physical modelling. *Chem. Eng. J.* **2023**, *480*, 147958. [CrossRef]
10. Grape, E.S.; Chacón-García, A.J.; Rojas, S.; Pérez, Y.; Jaworski, A.; Nero, M.; Åhlén, M.; Martínez-Ahumada, E.; Feindt, A.E.G.; Pepillo, M.; et al. Removal of pharmaceutical pollutants from effluent by a plant-based metal–organic framework. *Nat. Water* **2023**, *1*, 433–442. [CrossRef]
11. Zhang, Y.; Qian, C.; Duan, J.; Liang, Y.; Luo, J.; Han, Y.; Hu, J.; Shi, F. Synthesis of HKUST-1 embedded in SBA-15 functionalized with carboxyl groups as a catalyst for 4-nitrophenol to 4-aminophenol. *Appl. Surf. Sci.* **2022**, *573*, 151558. [CrossRef]
12. Zayeri, S.; Asl, S.; Mehrasa, S.; Saboor, F.; Safajoo-Jahankhanemlou, M. Safajoo-Jahankhanemlou, Inhibition Semiconductor Gas Sensors Based on Hollow Metal Oxides: Focusing on MOF-Derived Structures. *Prog. Chem. Biochem. Res.* **2025**, *8*, 304–329.
13. Biswas, B. A Review on the Synthesis of Metal-Organic Frameworks: Conventional, Unconventional, and Alternative Methods. *Res. Rev. Int. J. Multidiscip.* **2021**, *6*, 217–222. [CrossRef]
14. Shamshad, J.; Rehman, R.U. Innovative approaches to sustainable wastewater treatment: A comprehensive exploration of conventional and emerging technologies. *Environ. Sci. Adv.* **2025**, *4*, 189–222. [CrossRef]
15. Silva, J.A. Advanced Oxidation Process in the Sustainable Treatment of Refractory Wastewater: A Systematic Literature Review. *Sustainability* **2025**, *17*, 3439. [CrossRef]
16. Hübner, U.; Spahr, S.; Lutze, H.; Wieland, A.; Rüting, S.; Gernjak, W.; Wenk, J. Advanced oxidation processes for water and wastewater treatment—Guidance for systematic future research. *Heliyon* **2024**, *10*, e30402. [CrossRef]
17. Mosaferi, M.; Céolin, D.; Rueff, J.-P.; Selles, P.; Odelius, M.; Björneholm, O.; Öhrwall, G.; Carniato, S. Fingerprint of Dipole Moment Orientation of Water Molecules in Cu^{2+} Aqueous Solution Probed by X-ray Photoelectron Spectroscopy. *J. Am. Chem. Soc.* **2024**, *146*, 9836–9850. [CrossRef]
18. Heo, C.Y.; Díaz-Ramírez, M.L.; Park, S.H.; Kang, M.; Hong, C.S.; Jeong, N.C. Solvent-Driven Dynamics: Crafting Tailored Transformations of Cu(II)-Based MOFs. *ACS Appl. Mater. Interfaces* **2024**, *16*, 9068–9077. [CrossRef]
19. Patterson, N.; Xiao, B.; Ignaszak, A. Polypyrrole decorated metal–organic frameworks for supercapacitor devices. *RSC Adv.* **2020**, *10*, 20162–20172. [CrossRef]
20. Hussain, S.; Aneggi, E.; Goi, D. Catalytic activity of metals in heterogeneous Fenton-like oxidation of wastewater contaminants: A review. *Environ. Chem. Lett.* **2021**, *19*, 2405–2424. [CrossRef]

21. Duan, C.; Yu, Y.; Li, F.; Wu, Y.; Xi, H. Ultrafast room-temperature synthesis of hierarchically porous metal–organic frameworks with high space–time yields. *CrystEngComm* **2020**, *22*, 2675–2680. [CrossRef]
22. Raptopoulou, C.P. Metal-Organic Frameworks: Synthetic Methods and Potential Applications. *Materials* **2021**, *14*, 310. [CrossRef]
23. Zulfiqar, A.; Miao, B.; Khan, F.; Ali, N.; Ahmed, S.; Rehman, W.; Asad, M.; Nawaz, M.A.; Mir, I.A.; Rasheed, L. Metal–Organic Framework (MOF)-Based Catalysts for Sustainable Energy Technologies: A Review. *Langmuir* **2025**, *41*, 24049–24077. [CrossRef] [PubMed]
24. Cai, G.; Yan, P.; Zhang, L.; Zhou, H.-C.; Jiang, H.-L. Metal–Organic Framework-Based Hierarchically Porous Materials: Synthesis and Applications. *Chem. Rev.* **2021**, *121*, 12278–12326. [CrossRef]
25. Yang, C.; Xue, Z.; Wen, J. Recent Advances in MOF-Based Materials for Remediation of Heavy Metals and Organic Pollutants: Insights into Performance, Mechanisms, and Future Opportunities. *Sustainability* **2023**, *15*, 6686. [CrossRef]
26. Xiao, J.; Guo, S.; Wang, D.; An, Q. Fenton-Like Reaction: Recent Advances and New Trends. *Chem. Eur. J.* **2024**, *30*, e202304337. [CrossRef]
27. Liu, J.; Li, Q.; Mao, F.; Wang, K.; Wu, H. 2D MOFs-based Materials for the Application of Water Pollutants Removing: Fundamentals and Prospects. *Chem. Asian J.* **2021**, *16*, 3585–3598. [CrossRef] [PubMed]
28. Wu, D.; Tian, N.; Sun, X.; Wang, M.; Huang, J.; Deng, H.; Yu, D.; Wu, M.; Ni, H.; Pei, K.; et al. Enhanced fenton-like catalysis by facilely prepared nano-scale NCFOH/HKUST composites with synergistic effect for dye degradation. *Mater. Chem. Phys.* **2021**, *258*, 123980. [CrossRef]
29. Balaji, S.; Guda, R.; Mandal, B.K.; Kasula, M.; Ubba, E.; Khan, F.R.N. Green synthesis of nano-titania (TiO2 NPs) utilizing aqueous Eucalyptus globulus leaf extract: Applications in the synthesis of 4 H-pyran derivatives. *Res. Chem. Intermed.* **2021**, *47*, 3919–3931. [CrossRef]
30. Zuo, S.; Guan, Z.; Yang, F.; Xia, D.; Li, D. Reactive oxygen species regulation and synergistic effect for effective water purification through Fenton-like catalysis on single-atom Cu–N sites. *J. Mater. Chem. A* **2022**, *10*, 10503–10513. [CrossRef]
31. Afshariazar, F.; Morsali, A. Mixed-valence metal–organic frameworks: Concepts, opportunities, and prospects. *Chem. Soc. Rev.* **2025**, *54*, 1318–1383. [CrossRef]
32. Dummer, N.F.; Sodiq-Ajala, Z.; Morgan, D.J.; Davies, T.E. Investigating the preparation of $Cu_3Mo_2O_9$ as a photocatalyst. *Catal. Commun.* **2022**, *163*, 106414. [CrossRef]
33. Lelong, A.; Sakli, A.; Zeinert, A.; Lejeune, M. Carbon copper thin films for discoloration of indigo carmine. *Vacuum* **2018**, *148*, 136–139. [CrossRef]
34. Naz, F.; Saeed, K. Fabrication of Reduced Band Gap Copper Oxide Photocatalysts with Enhanced Dye Degradation under Visible Light. *J. Mater. Eng. Perform.* **2025**, *34*, 14520–14534. [CrossRef]
35. Kuncser, A.C.; Rostas, A.M.; Zavoianu, R.; Pavel, O.D.; Vlaicu, I.D.; Badea, M.; Culita, D.C.; Tirsoaga, A.; Olar, R. Synthesis and Characterization of Hematite-Based Nanocomposites as Promising Catalysts for Indigo Carmine Oxidation. *Nanomaterials* **2022**, *12*, 2511. [CrossRef] [PubMed]
36. Jegadeeswaran, P.; Rajiv, P.; Vanathi, P.; Rajeshwari, S.; Venckatesh, R. A novel green technology: Synthesis and characterization of Ag/TiO2 nanocomposites using Padina tetrastromatica (seaweed) extract. *Mater. Lett.* **2016**, *166*, 137–139. [CrossRef]
37. Yang, J.; Yang, W.; Zhang, C.; Gong, J.; Xu, M.; Li, J.; Liu, C. Synergistic self-driven and heterogeneous effect of a biomass-derived urchin-like Mn_3O_4/C_3N_4 Janus micromotor catalyst for efficient degradation of carbamazepine. *RSC Adv.* **2024**, *14*, 28904–28914. [CrossRef]
38. Saravanan, S.; Balamurugan, M.; Lippitz, A.; Fonda, E.; Swaraj, S. XANES studies of titanium dioxide nanoparticles synthesized by using Peltophorum pterocarpum plant extract. *Phys. B Condens. Matter* **2016**, *503*, 86–92. [CrossRef]
39. Karelius, K.; Ediati, R.; Santoso, E.; Santoso, U.T.; Faaizatunnisa, N.; Salsabila, R.A.; Pasaribu, M.H.; Agnestisia, R. Synthesis of MIL-100(Fe) derived α-Fe_2O_3 for fabrication of α-Fe_2O_3/ZIF-8 as photocatalyst of malachite green degradation. *Case Stud. Chem. Environ. Eng.* **2026**, *13*, 101320. [CrossRef]
40. Wang, R.; Xu, H.; Liu, X.; Fang, D.; Wei, S.; Yu, A.-N. In-situ growth of iron oxides with MIL-100(Fe) enhances its adsorption for selenite. *Surf. Interfaces* **2022**, *34*, 102325. [CrossRef]
41. Faaizatunnisa, N.; Lestari, W.W.; Saputra, O.A.; Saraswati, T.E.; Larasati, L.; Wibowo, F.R. Slow-Release of Curcumin Induced by Core–Shell Mesoporous Silica Nanoparticles (MSNs) Modified MIL-100(Fe) Composite. *J. Inorg. Organomet. Polym. Mater.* **2022**, *32*, 1744–1754. [CrossRef]
42. Ma, X.; Zhu, B.; Li, Z.; Wang, M.; Miao, C.-Q.; Liu, Y.; Zhang, S. Environmentally friendly synthesis of quasi-MIL-100(Fe) with modulation defects for efficient photo-Fenton degradation of ciprofloxacin. *Sep. Purif. Technol.* **2025**, *363*, 131990. [CrossRef]
43. Liang, X.; Li, L.; Wu, Y.; Liu, F.; Wang, Y.; Wu, Y.-H. Magnetic Recyclable Fe_3O_4/MOS_2@ Mil-100 (Fe) Ternary Catalyst for Photo-Fenton Degradation of Oxytetracycline Hydrochloride. *J. Alloys Compd.* **2025**, *1038*, 182610. [CrossRef]
44. Mirbagheri, N.S.; Heizmann, P.A.; Trouillet, V.; Büttner, J.; Fischer, A.; Vierrath, S. Adsorptive and photo-Fenton properties of bimetallic MIL-100(Fe,Sn) and MIL-100(Fe,Ir) MOFs toward removal of tetracycline from aqueous solutions. *Mater. Adv.* **2024**, *5*, 5724–5737. [CrossRef]

45. Miceli, M.; Frontera, P.; Macario, A.; Malara, A. Recovery/Reuse of Heterogeneous Supported Spent Catalysts. *Catalysts* **2021**, *11*, 591. [CrossRef]
46. Meng, J.; Ashry, A.G.; Abou-Elyazed, A.S.; Zhang, Z.; Li, X.; Sharara, T.Z.; El-Demerdash, S.H. Highly Efficient Visible-Light Photocatalysts: Bi_2O_3@TiO_2 Derived from Ti-MOFs for Eriochrome Black T Degradation: A Joint Experimental and Computational Study. *Catalysts* **2024**, *14*, 829. [CrossRef]
47. Usman, M.; Khan, K.I.; Adnan, M.; Khan, A. Facile synthesis of NiAl-LDH/Ag/g-C_3N_4 ternary composite for photocatalytic degradation of methylene blue. *Fuller. Nanotub. Carbon Nanostructures* **2023**, *32*, 264–273. [CrossRef]
48. Xiao, J.; Li, Y.; Dong, H.; Pang, Z.; Zhao, M.; Dong, J.; Huang, D.; Li, L. Iodide ion as an electron shuttle to significantly accelerate the elimination of sulfamethazine in the Fenton-like system under neutral condition. *Appl. Catal. B Environ.* **2024**, *344*, 123610. [CrossRef]
49. Waghmode, M.S.; Sahoo, D.K.; Patil, N.N.; Abhyankar, P.S.; Chirra, S.; Sohajda, T. Unveiling the environmental threat of acetaminophen: Ecotoxicology, microbial remediation, and molecular modelling insights. *Environ. Monit. Assess.* **2025**, *197*, 1326. [CrossRef]
50. Harvey, P.D. Porphyrin-based MOFs as heterogeneous photocatalysts for the eradication of organic pollutants and toxins. *J. Porphyr. Phthalocyanines* **2021**, *25*, 583–604. [CrossRef]
51. Ghorbani, P.; Mojtabapour, Z.S.; Ganjali, F.; Asl, F.R.; Forouzandeh-Malati, M.; Rashvandi, Z.; Kashtiaray, A.; Esmailzadeh, F.; Zarei-Shokat, S.; Taheri-Ledari, R.; et al. A light-driving magnetic nanocomposite based on Zn/Fe/Cu embedded in HKUST-1 applied for adsorption/degradation of Indigo carmine and pathogens. *Environ. Technol. Innov.* **2023**, *32*, 103439. [CrossRef]
52. Schlachter, A.; Asselin, P.; Harvey, P.D. Porphyrin-containing MOFs and COFs as heterogeneous photosensitizers for singlet oxygen-based antimicrobial nanodevices. *ACS Appl. Mater. Interfaces* **2021**, *13*, 26651–26672. [CrossRef]
53. Gupta, K.; Saini, K.; Shekhawat, K.S.; Mathur, J. Bio-inspired synthesis of Ag/TiO2 nanocomposites: Catalytic applications in tetraketone synthesis and anticancer activity on the MCF-7 cell line. *Res. Chem. Intermed.* **2025**, *51*, 3125–3153. [CrossRef]
54. Tony, M.A. Paradigms of homo/heterogonous Fenton systems incorporating 'Solar Energy' based on 'Emerging Pollutants' removal– challenges, advancements and visualized bibliometric analysis. *Int. J. Environ. Anal. Chem.* **2021**, *103*, 7877–7908. [CrossRef]
55. Thomas, N.; Dionysiou, D.D.; Pillai, S.C. Heterogeneous Fenton catalysts: A review of recent advances. *J. Hazard. Mater.* **2021**, *404*, 124082. [CrossRef]
56. Wu, T.; Li, X.; Weng, C.-H.; Ding, F.; Tan, F.; Duan, R. Highly efficient LaMO3 (M = Co, Fe) perovskites catalyzed Fenton's reaction for degradation of direct blue 86. *Environ. Res.* **2023**, *227*, 115756. [CrossRef]

Disclaimer/Publisher's Note: The statements, opinions and data contained in all publications are solely those of the individual author(s) and contributor(s) and not of MDPI and/or the editor(s). MDPI and/or the editor(s) disclaim responsibility for any injury to people or property resulting from any ideas, methods, instructions or products referred to in the content.